

## JGR Solid Earth

## RESEARCH ARTICLE

10.1029/2022JB024432

## Interpretation of Anhyseretic Remanent Magnetization Carriers in Magnetofossil-Rich Marine Sediments

Qiang Zhang<sup>1</sup> , Andrew P. Roberts<sup>2</sup> , Shulan Ge<sup>3,4</sup> , Yanguang Liu<sup>3,4</sup> , Jianxing Liu<sup>3,4</sup>,  
Shuangchi Liu<sup>1</sup>, Xu Tang<sup>1</sup> , Haosen Wang<sup>5</sup> , Dunfan Wang<sup>5</sup>, Jinhua Li<sup>1</sup> , and Qingsong Liu<sup>5</sup> 

<sup>1</sup>State Key Laboratory of Lithospheric Evolution, Institute of Geology and Geophysics, Chinese Academy of Sciences, Beijing, China, <sup>2</sup>Research School of Earth Sciences, Australian National University, Canberra, ACT, Australia, <sup>3</sup>Key Laboratory of Marine Geology and Metallogeny, First Institute of Oceanography, MNR, Qingdao, China, <sup>4</sup>Laboratory for Marine Geology, Pilot National Laboratory for Marine Science and Technology, Qingdao, China, <sup>5</sup>Department of Ocean Science and Engineering, Southern University of Science and Technology, Shenzhen, China

## Key Points:

- Integrated component analyses are presented for four sediment cores to identify magnetic particle sources
- Magnetofossils are the predominant anhyseretic remanent magnetization (ARM) carrier with detrital and extracellular magnetite also contributing to the ARM
- Quantitative analyses provide valuable insights into the nature of components to improve ARM data interpretation of marine sediments

## Correspondence to:

Q. Zhang and Q. Liu,  
zqwy163@163.com;  
qslu@sustech.edu.cn

## Citation:

Zhang, Q., Roberts, A. P., Ge, S., Liu, Y., Liu, J., Liu, S., et al. (2022). Interpretation of anhyseretic remanent magnetization carriers in magnetofossil-rich marine sediments. *Journal of Geophysical Research: Solid Earth*, 127, e2022JB024432. <https://doi.org/10.1029/2022JB024432>

Received 22 MAR 2022

Accepted 8 NOV 2022

## Author Contributions:

**Conceptualization:** Qiang Zhang**Methodology:** Qiang Zhang, Shuangchi Liu, Xu Tang, Jinhua Li**Resources:** Shulan Ge, Yanguang Liu, Jianxing Liu, Haosen Wang, Dunfan Wang**Visualization:** Qiang Zhang**Writing – original draft:** Qiang Zhang**Writing – review & editing:** Qiang Zhang, Andrew P. Roberts, Qingsong Liu

**Abstract** The anhyseretic remanent magnetization (ARM) is an important magnetic parameter for quantifying the concentration of “fine”, mostly sub-micron ferrimagnetic particles in rocks and sediments. A sound understanding of ARM carriers is needed to interpret magnetic and environmental information in sedimentary archives. This is often not achieved for marine sediments, which routinely contain several magnetic mineral components. Here, we analyze marine sediment records over different timescales for four sediment cores from the Eastern Pacific Ocean (Hole 1218A), the Antarctic margin (core P4-1), the Arctic Ocean (core ARC5-ICE4), and the South China Sea (core L07), using coercivity spectra analyses of ARM, first-order reversal curve principal component analysis (FORC-PCA), transmission electron microscopy (TEM), and unmixing of isothermal remanent magnetization (IRM) curves. By combining rock magnetic and TEM results, we find that the ARM is mainly carried by non-interacting single domain (SD) biogenic magnetite (magnetofossils) in the studied sediments over all timescales. Low-coercivity magnetic particles (detrital and fine-grained extracellular magnetite) also contribute to the bulk ARM. Variable magnetofossil chain structures are detected and have a significant influence on ARM data interpretation. Quantitative FORC-PCA endmember analyses based on quantile contours and coercivity distributions provide valuable information on the nature of endmembers and improve ARM data interpretation. We provide an integrated strategy to help reduce interpretational ambiguities related to ARM in future studies.

**Plain Language Summary** The anhyseretic remanent magnetization (ARM) is an important parameter that is used to assess information about Earth's magnetic field variations and environmental changes. To interpret ARM signals robustly, we must understand the sedimentary magnetic minerals that control ARM changes. However, the origin of ARM changes in marine sediments is not well understood. Here, we analyze marine sediment records from the Eastern Pacific Ocean, the Antarctic margin, the Arctic Ocean, and the South China Sea to identify the carriers of ARM in the respective sediments. Our results indicate that all of the sediments contain abundant remains of magnetotactic bacteria (known as magnetofossils). Magnetofossil abundance variations dominate ARM on both 10,000 to million-year timescales. Part of the bulk ARM is also contributed by other low-coercivity magnetite particles. Furthermore, ARM is influenced significantly by magnetofossil chain structure variations. Our results have important implications for future studies involving use of ARM in magnetofossil-rich sediments.

## 1. Introduction

The anhyseretic remanent magnetization (ARM) is a laboratory-imparted artificial remanence that is used widely in mineral magnetic studies (Dunlop & Özdemir, 1997). An ARM is usually imparted by exposing a sample to an alternating field (AF; e.g., ~100 mT) with a superimposed small direct current (DC; e.g., ~50  $\mu$ T) bias field. The bulk ARM is given as the sum of the ARM of each component (Egli, 2004a, 2004b; Fabian & Leonhardt, 2009):

$$M_{ar} = H_{dc} \sum_{i=1}^N M_{rsi} \kappa_i, \quad (1)$$

where  $M_{ar}$  is the bulk ARM imparted with a DC field  $H_{dc}$  for a sample containing  $N$  magnetic components with saturation remanence  $M_{rs}$  and component-specific ARM ratios,  $\kappa_i = \chi_{ai} / M_{rsi}$ , where  $\kappa_i$  is the ratio of the ARM

© 2022. The Authors.

This is an open access article under the terms of the [Creative Commons Attribution-NonCommercial-NoDerivs License](https://creativecommons.org/licenses/by-nc-nd/4.0/), which permits use and distribution in any medium, provided the original work is properly cited, the use is non-commercial and no modifications or adaptations are made.

susceptibility  $\chi_{ai}$  to  $M_{rsi}$  for the  $i$ th component. Stable single domain (SD) particles acquire a larger ARM than multi-domain (MD) particles (Maher, 1988). ARM is also an important parameter for normalizing the natural remanent magnetization (NRM) to estimate the geomagnetic relative paleointensity (RPI) using NRM/ARM (Channell et al., 2014, 2018; Johnson et al., 1975; King et al., 1983; Levi & Merrill, 1976; Macri et al., 2005; Pan et al., 2001; Richter et al., 2006; Stoner et al., 2000, 2003; Tauxe et al., 1995; Tauxe & Yamazaki, 2015; Yamamoto et al., 2007; Yamazaki & Yamamoto, 2018; Zhu et al., 2000). In this case, ARM provides a measure of the concentration of NRM carrier particles in a sample so that NRM/ARM is used as a measure of ancient geomagnetic field strength variations (e.g., King et al., 1983; Roberts et al., 2013; Tauxe, 1993). The ratio of ARM to bulk susceptibility or to isothermal remanent magnetization (IRM) is also used commonly in magnetic studies (Arnold et al., 1995; Banerjee et al., 1981; Channell et al., 2016; Dunlop & Özdemir, 1997; Evans & Heller, 2003; Florindo et al., 2013; Ge et al., 2012; Hunt et al., 1995; King et al., 1982; Larrasoña et al., 2012; Maher, 2011; Nie et al., 2013; Thompson & Oldfield, 1986; Torrent et al., 2007). The ARM to isothermal remanent magnetization (IRM) ratio can be expressed as due to  $N$  components:

$$\frac{M_d}{M_{rs}} = H_{dc} \frac{\sum_{i=1}^N M_{rsi} \chi_i}{\sum_{i=1}^N M_{rsi}}. \quad (2)$$

Depending on which component dominates the magnetic mineral assemblage,  $M_d/M_{rs}$  might be controlled by grain size (e.g., sediments dominated by a detrital component; Banerjee et al., 1981; Dunlop & Özdemir, 1997; King et al., 1982; Thompson & Oldfield, 1986), magnetostatic interactions (e.g., among magnetic inclusions within silicate host minerals; Chang, Roberts, et al., 2016), configurational anisotropy (e.g., magnetofossils with different chain structures; Amor et al., 2022; Li et al., 2012; Moskowitz et al., 1993; Pan et al., 2005), or a combination of these factors. ARM-related parameters can, therefore, provide considerable magnetic and environmental information from natural archives. It is necessary to understand the magnetic components responsible for ARM changes before interpreting such information.

Globally distributed marine sediments are an important target of paleomagnetic and environmental magnetic studies. Vali et al. (1989) studied sediments from the Pacific and Atlantic Oceans to explore magnetic mineral compositions related to ARM variations. By comparing ARM demagnetization curves and their gradients, they defined three groups of ARM carriers. SD magnetofossils were the main ARM carrier, while volcanically sourced vortex state/MD magnetite-titanomagnetite within rock fragments, and a group with a distribution of vortex state/MD detrital phases with intermediate magnetic properties between those of the first two groups were identified as the main ARM carriers. In the western equatorial Pacific Ocean (ODP Site 805), biogenic magnetite near the Fe-redox boundary was verified to be the main ARM carrier by coercivity analysis (Tarduno et al., 1998). Egli (2004a) performed a more detailed analysis of ARM and IRM demagnetization curves using model functions on samples from various environments (i.e., lacustrine and marine sediments, limestone, loess, soils, and eolian dust). Eight magnetic component groups were identified by unmixing ARM demagnetization curves, including: low- and high-coercivity biogenic magnetite, low-coercivity detrital particles (D) and extracellular magnetite (EX), a pedogenic component (PD), urban pollution (UP), and high-coercivity maghemite (eolian dust, ED) and imperfect antiferromagnetic components (H). Detrital particles and fine extracellular magnetite (D+EX), with two biogenic magnetite components were identified by Egli (2004a) in a marine sediment sample (pelagic carbonate, ODP Leg 182). Complicated magnetic mineral assemblages, with nine particle classes identified by electron microscope observations in equatorial Atlantic Ocean sediments, also provide information on ARM-related parameter variations, including the effects of mineralogy and source-to-sink processes (Franke et al., 2007). These studies demonstrate that identifying ARM carriers and interpreting ARM signals are not straightforward for magnetically multi-component marine sediments.

Fossilized biogenic magnetite (Kirschvink & Chang, 1984; Larrasoña et al., 2012; Roberts et al., 2011; Vali et al., 1989; Yamazaki, 2012) produced in situ by magnetotactic bacteria (MTB) (Bazylnski & Frankel, 2004; Faivre & Schüler, 2008; Kopp & Kirschvink, 2008; Vali et al., 1987; von Dobeneck et al., 1987) occurs within the narrow SD grain size range. Hence, ARM is highly sensitive to magnetofossils. Although SD biogenic magnetite is an ideal ARM carrier, magnetofossil ARM characteristics can also be influenced significantly by the shape and collapse of their chain structures (Amor et al., 2022; Berndt et al., 2020; Li et al., 2012; Moskowitz et al., 1993; Pan et al., 2005), which complicates ARM interpretation.

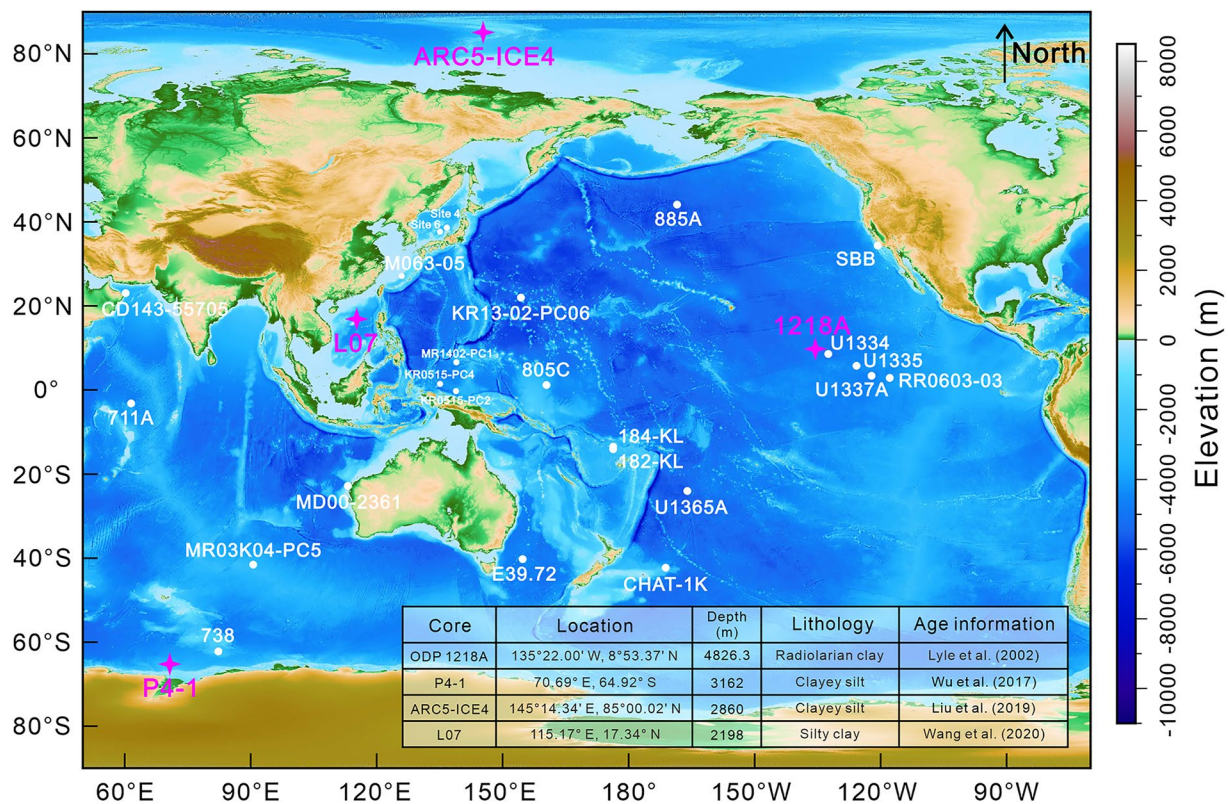


**Figure 1.** Location map of cores studied here. Also shown are sites from which magnetofossil records have been reported, including Sites 4 and 6 (Yamazaki et al., 2019), core KR13-02-PC06 (Yamazaki et al., 2020), IODP Hole U1365A (Yamazaki & Shimono, 2013), cores KR0515-PC2 and PC4 (Yamazaki & Horiuchi, 2016), core MR1402-PC1 (Sakuramoto et al., 2017), ODP Hole 805C (Tarduno et al., 1998), cores 182/184-KL (Vali et al., 1987), core MD00-2361 (Heslop et al., 2013), core M063-05 (Li et al., 2019), core E39.72 (Hesse, 1994), core CHAT-1K (Lean & McCave, 1998), IODP Sites U1334 and U1335 (Channell et al., 2013), IODP Hole U1337A (Yamazaki, 2012), core RR0603-03 (Chen et al., 2017), Site SBB (Santa Barbara Basin) (Stolz et al., 1986), core CD143-55705 (Chang, Heslop, et al., 2016), ODP Hole 711A (Chang et al., 2012), core MR03K04-PC5 (Yamazaki & Ikehara, 2012), ODP Site 738 (Larrasoana et al., 2012; Roberts et al., 2011), and ODP Hole 885A (Zhang et al., 2021). Details of the studied cores are indicated in the inset table.

Marine sediments contain complex magnetic mineral mixtures with different origins and magnetic properties (e.g., Egli, 2004a; Franke et al., 2007; Li et al., 2020). Magnetic unmixing is often used to identify the remanence carrier for each component (e.g., Heslop, 2015). ARM demagnetization and component analysis are effective for this purpose (Egli, 2004a; Tarduno et al., 1998; Vali et al., 1989). First-order reversal curve (FORC) diagrams (Pike et al., 1999; Roberts et al., 2000) provide further information to discriminate among magnetic particles with different domain states (superparamagnetic, SD, vortex state, and MD) and origins (e.g., biogenic and detrital). Quantitative information about these magnetic mineral types can be obtained from FORC-principal component analysis (FORC-PCA) (Harrison et al., 2018; Lascau et al., 2015). Due to its numerical stability (as a linear spectral method) and use of a 2D parameter space, FORC-PCA has become a preferred method for numerical magnetic unmixing of marine sediments (Channell et al., 2016; Inoue et al., 2021; Qian et al., 2020; Roberts et al., 2018; Wagner et al., 2021; Yamazaki et al., 2020; Zhang et al., 2021).

In this study, we seek to identify ARM carriers in marine sediment cores from the Eastern Pacific Ocean, the Antarctic margin, the Arctic Ocean, and the South China Sea (Figure 1). We present ARM component analysis, FORC-PCA, transmission electron microscopy (TEM), and IRM unmixing results for samples from these cores. By comparing variations over tectonic and orbital timescales, we clarify magnetic component variations responsible for ARM changes in these samples.

## 2. Materials and Methods

### 2.1. Materials

In this study, 86 discrete sediment samples were analyzed from Eastern Pacific Ocean Drilling Program (ODP) Hole 1218A (Lyle et al., 2002), Antarctic margin core P4-1 (Wu et al., 2017), Arctic Ocean core ARC5-ICE4 (Liu et al., 2019), and South China Sea core L07 (Wang et al., 2020). Relevant details for each sediment core are shown in Figure 1.

### 2.2. Methods

An ARM was imparted to samples from ODP Hole 1218A and cores P4-1 and ARC5-ICE4 in a 100-mT AF with a superimposed 50  $\mu$ T DC bias field using a 2-G Enterprises Model 760-R cryogenic magnetometer with inline demagnetization system in a shielded room. ARM data for core L07 are from Wang et al. (2020). AF demagnetization of ARM is based on Egli (2004a), with 54 stepwise increasing peak AFs applied up to 100 mT along the same direction to which the ARM was imparted. The steps are distributed on a nearly logarithmic scale (1 mT steps for 0–20 mT, 1.5 mT steps for 21.5–26 mT, 2 mT steps for 28–72 mT, 3 mT steps for 74–80 mT, 5 mT steps for 85–100 mT). ARM AF demagnetization curves were then analyzed using the MAG-MIX software (Coercivity Distribution Analyzer (CODICA) and Generalized Coercivity Analyzer (GECA)) in Mathematica (Egli, 2003, 2004a).

FORCs were measured for all samples using a Princeton Measurements Corporation MicroMag 3900 vibrating sample magnetometer (VSM), with 100 FORCs measured per sample, a 500 ms averaging time, and 1 T maximum applied field. For Hole 1218A samples,  $B_c$  ranged between 0 and 150 mT and  $B_u$  between –40 and +40 mT. For cores P4-1 and ARC5-ICE4,  $B_c$  ranged between 0 and 200 mT and  $B_u$  between –80 and +80 mT. For core L07,  $B_c$  ranged between 0 and 150 mT and  $B_u$  between –60 and +60 mT. FORC data were imported into the FORCinel software (version 3.06; Harrison & Feinberg, 2008) for FORC-PCA with VARIFORC smoothing (Egli, 2013). Quantitative FORC analyses (quantile contours and coercivity distributions) were produced for extracted FORC EMs using VARIFORC (Egli, 2013, 2021). IRM curves for representative samples were measured with the VSM. IRM unmixing was then conducted with the MAG-MIX software (Egli, 2003, 2004a).

Magnetic minerals were extracted from representative bulk sediments following Zhang et al. (2018). Microscopic analysis of magnetic extracts and magnetofossil identification were performed with a TEM following Li et al. (2020). Two-dimensional morphologies of targets were imaged and recorded with a JEOL 2100 TEM at 200 kV. The chemical composition and mineralogy of individual particles were analyzed with energy-dispersive X-ray spectroscopy (EDXS) and selected area electron diffraction (SAED), respectively.

## 3. Results

### 3.1. ARM Variations

Bulk ARM variations for samples from each core are shown in Figures 2a-1 to 2d-1. For the longer and older Eastern Pacific Ocean Hole 1218A record, the mean ARM value ( $72.61 \times 10^{-5}$  Am<sup>2</sup>/kg) is much higher than in the other cores, with a decreasing trend and high-amplitude fluctuations since the late Miocene (ARM<sub>Bulk</sub>, Figure 2a-1). For Antarctic margin core P4-1, ARM<sub>Bulk</sub> has characteristic glacial-interglacial variations over the past 500 ka and a  $19.2 \times 10^{-5}$  Am<sup>2</sup>/kg mean value (Figure 2b-1). For Arctic Ocean core ARC5-ICE4, the mean ARM<sub>Bulk</sub> value is  $4.77 \times 10^{-5}$  Am<sup>2</sup>/kg for the past 2.6 Ma. ARM<sub>Bulk</sub> increased gradually from 2.6 to 1.0 Ma, and then dropped between 1.0 and 0.4 Ma; thereafter, it rose again (Figure 2c-1). For South China Sea core L07, ARM<sub>Bulk</sub> has a generally increasing trend over the past 40 ka with a mean value of  $9.25 \times 10^{-5}$  Am<sup>2</sup>/kg (Figure 2d-1).

### 3.2. ARM Component Analysis

ARM component analysis results for each core are shown in Figure 3. All samples in the four cores can be modeled with four magnetic components. The first is a low-coercivity (LC) component with magnetic properties close to those of the mixed detrital and fine-grained extracellular magnetite (D + EX) of Egli (2004a), which cannot be disentangled, due to their similar coercivity distributions. The second and the third components have

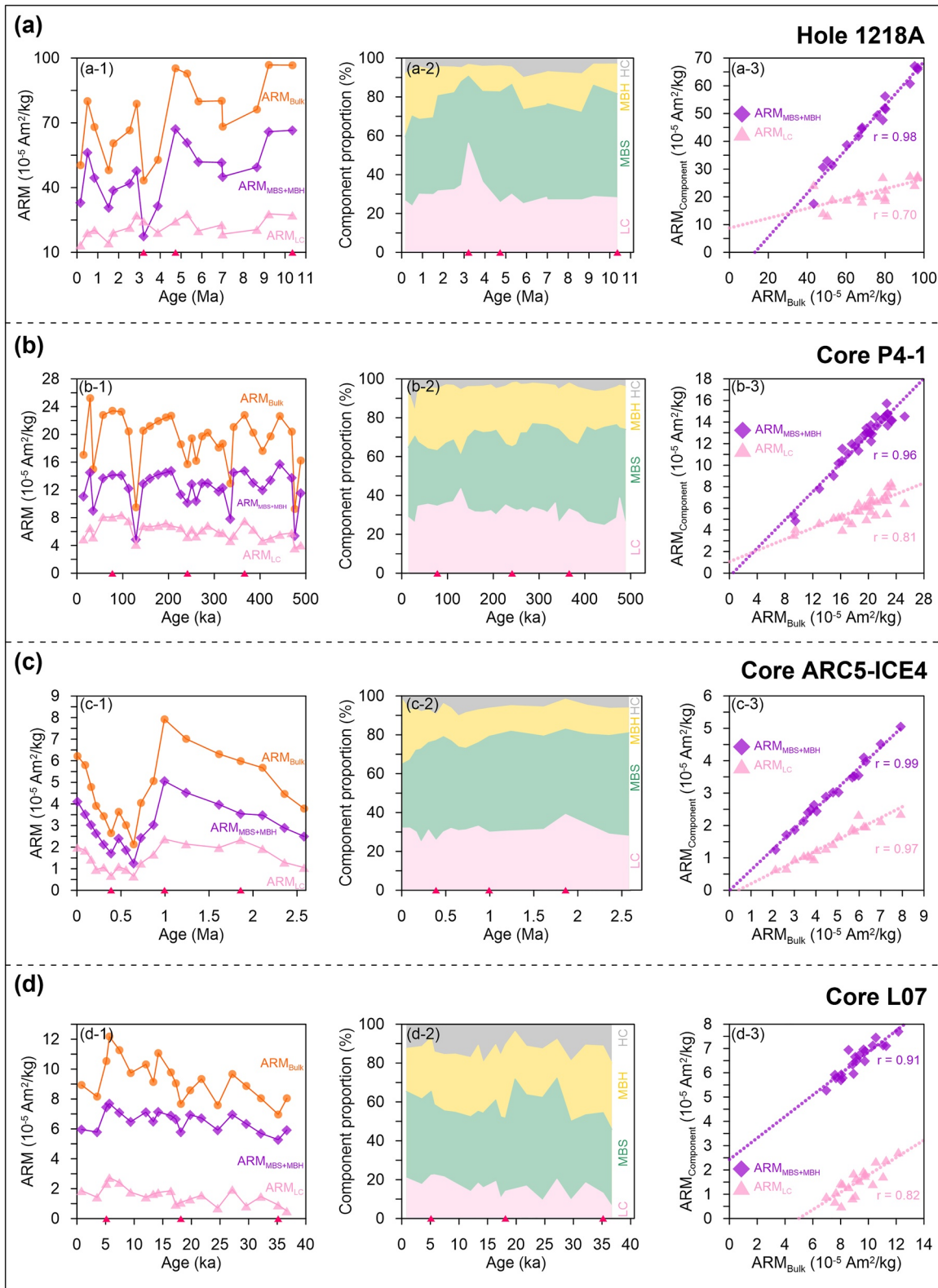


**Figure 2.** Comparison between ARM component analysis results and bulk ARM ( $\text{ARM}_{\text{Bulk}}$ ). (a-1 to d-1) Variation of  $\text{ARM}_{\text{Bulk}}$ , ARM carried by MBS + MBH ( $\text{ARM}_{\text{MBS+MBH}}$ ), and low-coercivity ( $\text{ARM}_{\text{LC}}$ ) components. (a-2 to d-2) Variations of component proportions obtained from ARM coercivity spectra. (a-3 to d-3) Correlation plots of  $\text{ARM}_{\text{MBS+MBH}}$  versus  $\text{ARM}_{\text{Bulk}}$  and  $\text{ARM}_{\text{LC}}$  versus  $\text{ARM}_{\text{Bulk}}$ . The correlation coefficient is  $r$ . Red triangles on the age axis indicate samples for which FORC diagrams are shown in Figure 5.

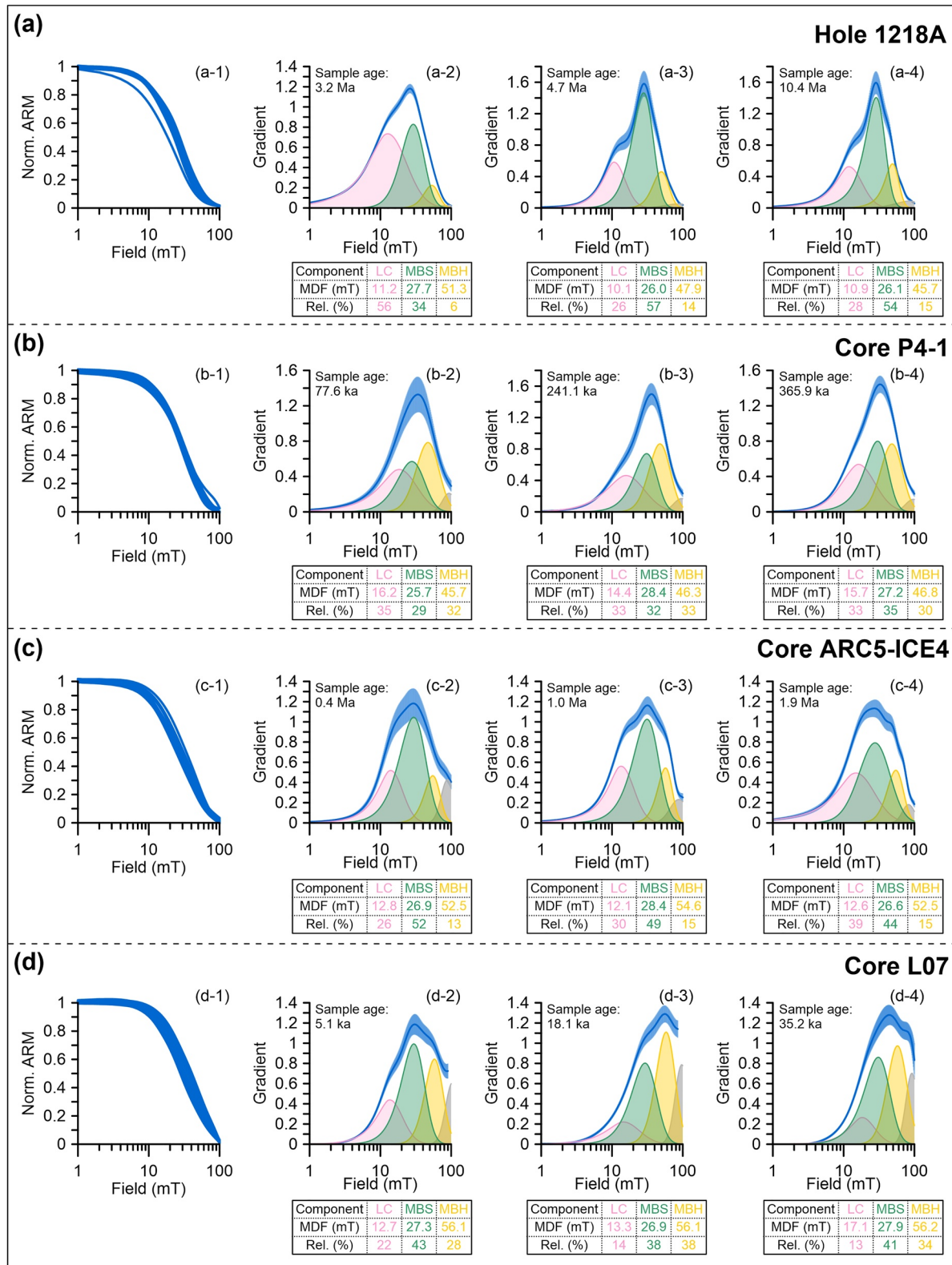


**Figure 3.** ARM component analysis results. The data were analyzed using the MAG-MIX software (CODICA and GECA). (a-1 to d-1) Normalized ARM demagnetization curves. (a-2 to a-4, b-2 to b-4, c-2 to c-4, d-2 to d-4) Coercivity distributions of ARM. The low-coercivity (LC), MBS, MBH, and high-coercivity (HC) components are labelled with pink, green, yellow, and gray, respectively. The sum coercivity distributions (blue) are plotted together with their confidence limits. The median destructive field (MDF) and relative contribution (Rel.) are shown in the respective tables. Information for HC is not shown here due to its incomplete definition due to the limited maximum AF used.

similar coercivity distributions to those of the BM (biogenic marine) and BI (biogenic intermediate) components identified in Southern Ocean (ODP Leg 182) pelagic carbonates by Egli (2004a). BM and BI are the marine counterparts of BS (biogenic soft) and BH (biogenic hard) from freshwater sediments, respectively; their 30% smaller MDFs are interpreted as due to differences in the magnetite produced by freshwater and marine magnetotactic bacteria strains (Egli, 2004a). To make it more specific, we use the terms marine biogenic soft (MBS) and marine biogenic hard (MBH) to refer to the BM and BI components, respectively, of Egli (2004a). The fourth component contains a variable high-coercivity (HC) contribution, which is more evident in core L07 (Figures 3d-2 to 3d-4). The HC component is unsaturated in the 100 mT maximum AF amplitude, especially for core L07; thus, separation of HC is poorly conditioned mathematically, which hampers its precise definition.

### 3.3. TEM Observations

TEM images of magnetic extracts from bulk sediments in each core are shown in Figure 4. Magnetofossils with equant and elongated morphologies are identified in Hole 1218A (Figures 4a-1 to 4a-6). From EDXS results, the magnetofossils contain Fe and O with no impurity elements (Figures 4a-7 to 4a-9) and corresponding SAED patterns (inserted diffraction diagrams in Figures 4a-1 and 4a-2) are consistent with the presence of magnetite. In this hole, equant magnetofossils are dominant compared to elongated forms (Figures 4a-10 to 4a-12). Abundant magnetofossils have been reported from Cenozoic eastern equatorial Pacific Ocean pelagic sediments (Channell et al., 2013; Chen et al., 2017; Yamazaki, 2012), where low organic carbon burial prevents reductive diagenesis, which aids bacterial magnetite preservation (Channell et al., 2013). The low organic carbon contents and oxic conditions are validated by the lithostratigraphy and pore water geochemistry at Site 1218 (Lyle et al., 2002).

For core P4-1, beside biogenic magnetite (Figures 4b-1 to 4b-5), submicron detrital minerals are detected in TEM observations (Figure 4b-6), which may be (titano)magnetite as indicated by the SAED pattern (diffraction diagram inset in Figure 4b-6) and elemental compositions (Figure 4b-9). Antarctic margin magnetofossil records have been obtained from Paleocene-Oligocene sediments at ODP Site 738, southern Kerguelen Plateau (Larrasoana et al., 2012; Roberts et al., 2011). We detect magnetofossils from even closer to the Antarctic continent in late Pleistocene sediments from core P4-1, Prydz Bay. Core P4-1 is located far from submarine canyons, so sediments are not affected by turbidity or debris flows, which ensures reasonably stable sedimentation (Wu et al., 2017). This condition is conducive to biogenic magnetite preservation.

The two magnetofossil types (Figures 4c-1 to 4c-5, 4d-1, 4d-2, 4d-4 to 4d-6) and submicron detrital (titano) magnetite (Figures 4c-6 and 4d-3) are also identified in cores ARC5-ICE4 and L07. No obvious diagenetic reduction has been identified in these two cores (Liu et al., 2019; Wang et al., 2020), and magnetofossils are well preserved. Core ARC5-ICE4 provides the first magnetofossil record from Arctic marine sediments. The core is from the eastern Lomonosov Ridge, central Arctic Ocean. Although there is less knowledge of the Cenozoic paleoceanography of the central Arctic Ocean than for any other ocean basin (Coakley et al., 2016), our results reveal that even polar environments provide suitable conditions for MTB biomineralization, and extend the reported geographical distribution of magnetofossils.

Elongated magnetofossils have been proposed to have higher coercivities than equant types (Chang et al., 2018; Egli, 2004a; Yamazaki et al., 2019, 2020; Zhang et al., 2021). Direct observation of these two magnetofossil types supports our ARM component interpretation. It also supports the interpretation that the coercivity of magnetite produced by marine MTB strains is smaller than that produced by freshwater strains (Egli, 2004a).

### 3.4. FORC-PCA

FORC diagrams for representative samples and FORC-PCA results are shown in Figure 5. For Hole 1218A, all FORC diagrams have characteristic central ridges with narrow vertical distributions (Figures 5a-4 to 5a-6). Two end members (EMs) with marked central ridges are evident in FORC-PCA results (Figures 5a-2 and 5a-3). Two EMs explain ~81% of the data variance. The  $B_c$  distribution of EM1 peaks at ~15–20 mT and extends to ~60 mT (Figure 5a-2), while that of EM2 peaks at ~30 mT and extends to ~80 mT (Figure 5a-3). FORC diagrams for these two EMs are typical of those for magnetostatically noninteracting SD particles (Egli et al., 2010; Pike et al., 1999; Roberts et al., 2000) associated with magnetofossils, as determined from selective chemical extraction (Ludwig et al., 2013) and micromagnetic calculations (Amor et al., 2022; Chang et al., 2019). The two

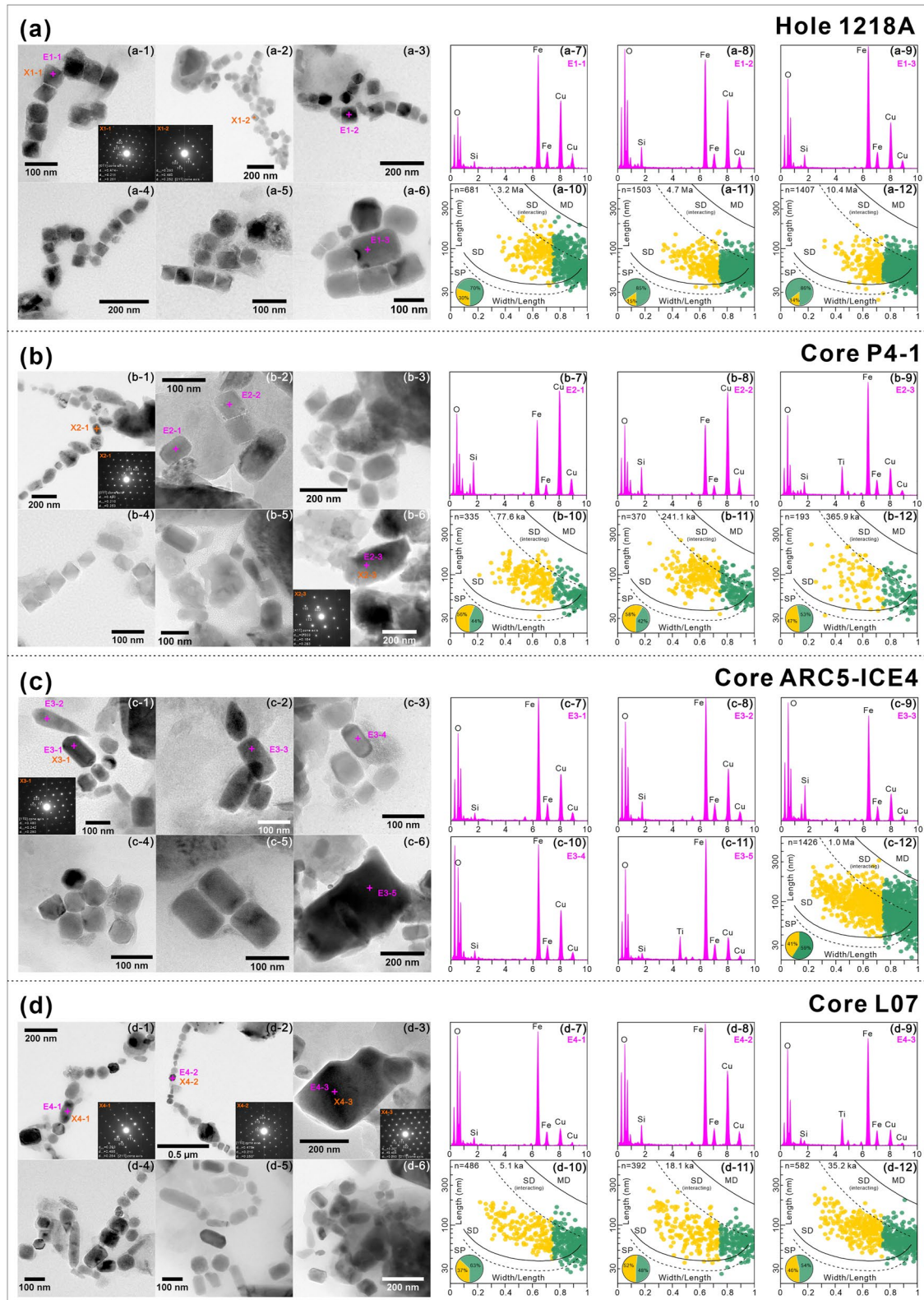


**Figure 4.** Transmission electron microscope (TEM) images for (a) Hole 1218A, and cores (b) P4-1, (c) ARC5-ICE4, and (d) L07. TEM images are shown in a-1 to a-6, b-1 to b-6, c-1 to c-6, and d-1 to d-6. Insets are selected area electron diffraction (SAED) patterns for the corresponding analysis points. Respective energy-dispersive X-ray spectroscopy (EDXS) results are shown in a-7 to a-9, b-7 to b-9, c-7 to c-11, and d-7 to d-9. Si and Cu signals are from nearby silicate particles and Cu grid, respectively. Magnetofossil size distributions are shown in a-10 to a-12, b-10 to b-12, c-12, and d-10 to d-12, where yellow and green symbols denote magnetofossils with elongated ( $\text{width/length} < 0.75$ ) and equant ( $0.75 < \text{width/length} < 1$ ) crystals, respectively (Kopp & Kirschvink, 2008); pie charts are the corresponding statistics.

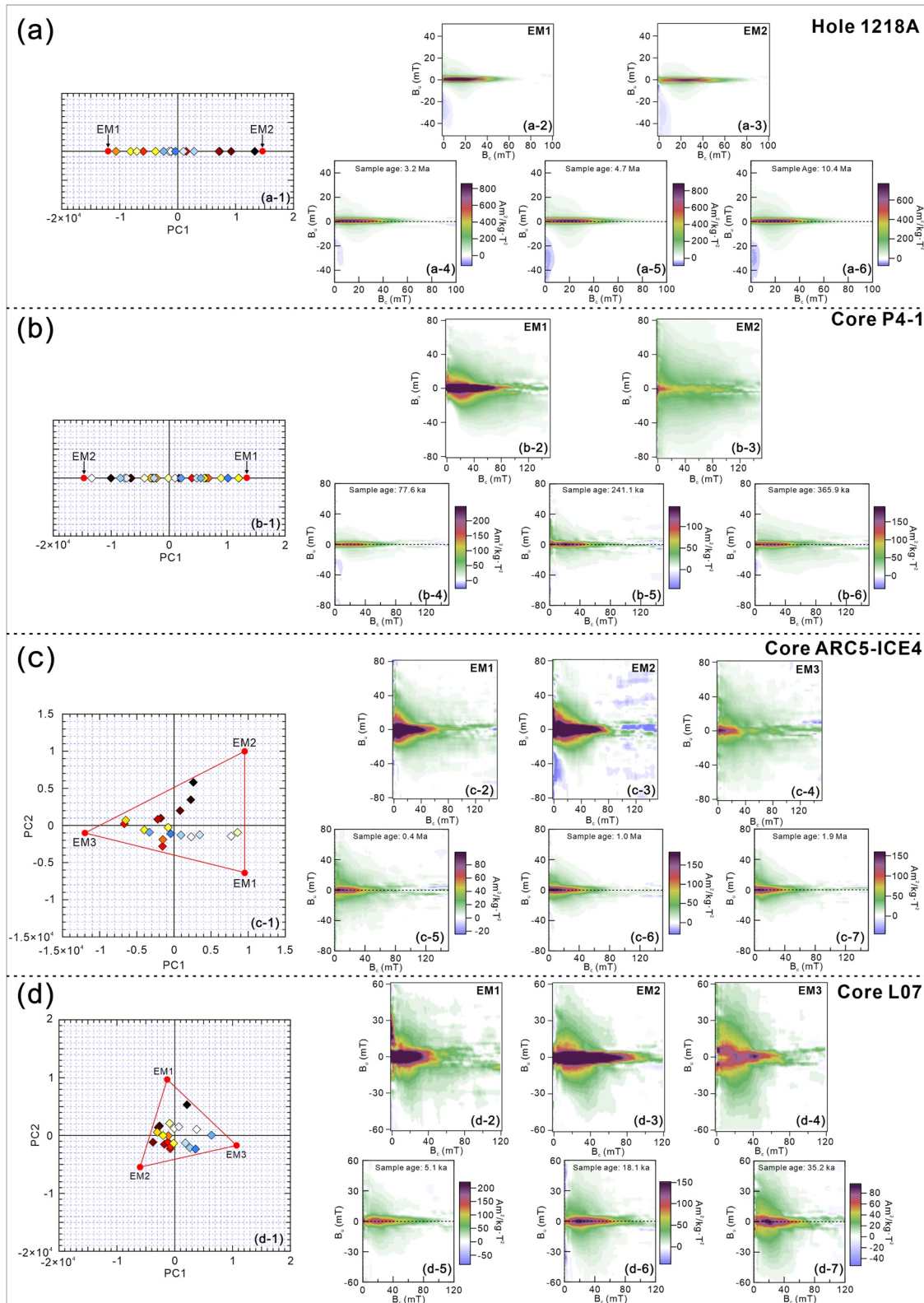


**Figure 5.** FORC-PCA results for (a) Hole 1218A (VARIFORC (Egli, 2013) smoothing parameters are:  $S_{c0} = 4$ ,  $S_{b0} = 3$ , and  $S_{c1} = S_{b1} = 7$ ); (b) core P4-1 ( $S_{c0} = 4$ ,  $S_{b0} = 3$ , and  $S_{c1} = S_{b1} = 7$ ); (c) core ARC5-ICE4 ( $S_{c0} = 5$ ,  $S_{b0} = 4$ , and  $S_{c1} = S_{b1} = 7$ ); and (d) core L07 ( $S_{c0} = 6$ ,  $S_{b0} = 5$ , and  $S_{c1} = S_{b1} = 9$ ). Principal component (PC) scores are shown for the samples in a-1 to d-1. End member (EM) FORC diagrams are shown in a-2, a-3, b-2, b-3, c-2, c-3, c-4, d-2, d-3, and d-4. FORC diagrams for representative samples are shown in a-4 to a-6, b-4 to b-6, c-5 to c-7, and d-5 to d-7.

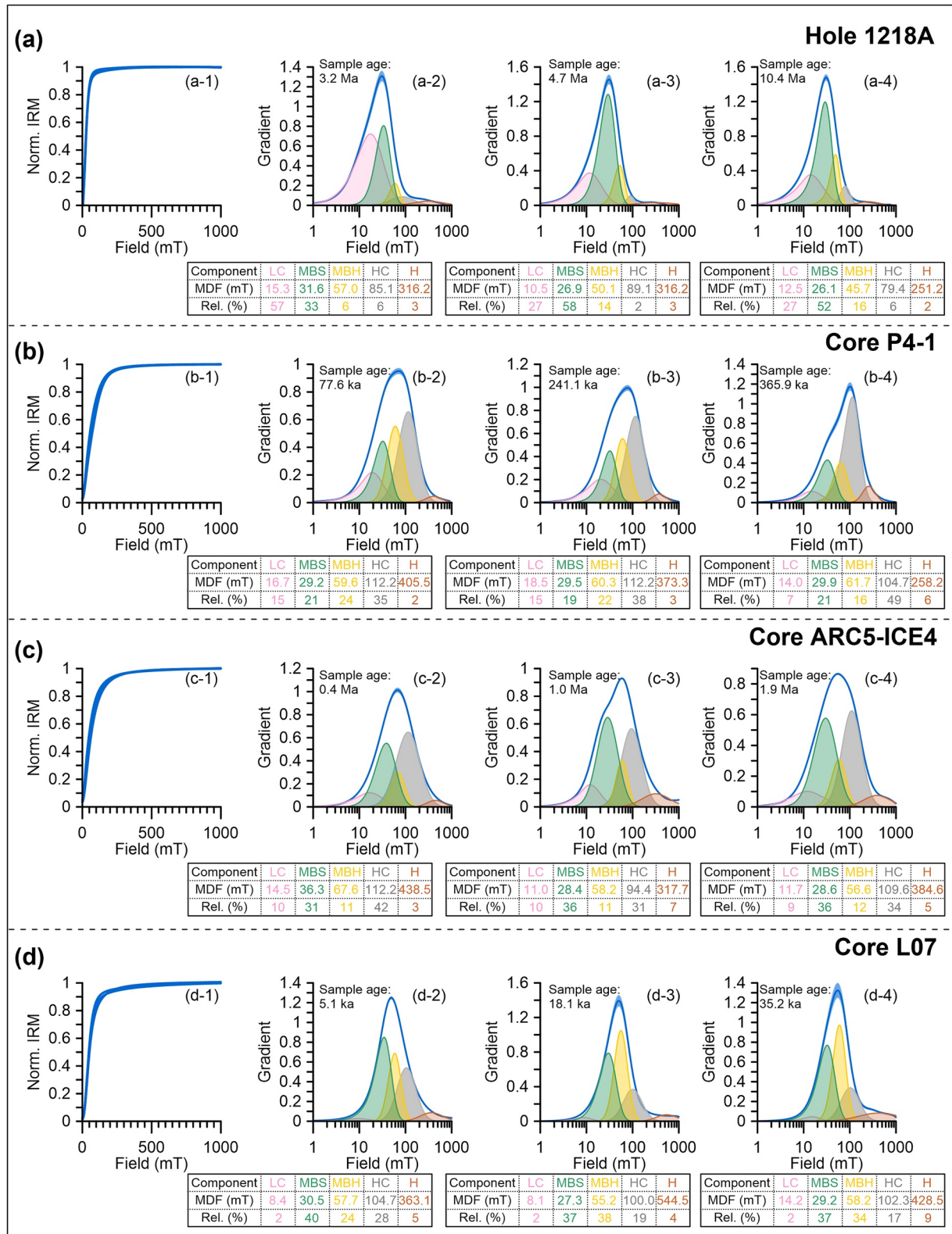


**Figure 6.** IRM unmixing results. The data were analyzed using the MAG-MIX software (CODICA and GECA). (a-1 to d-1) Normalized IRM acquisition curves. (a-2 to a-4, b-2 to b-4, c-2 to c-4, and d-2 to d-4) Coercivity distributions of IRM. The low-coercivity (LC), MBS, MBH, high-coercivity (HC), and hematite (H) components are labelled with pink, green, yellow, gray, and brown, respectively. The sum of coercivity distributions (blue) are plotted together with their confidence limits. The median destructive field (MDF) and relative contribution (Rel.) are shown in the respective tables.

**Table 1**  
 $\chi_{ARM}/IRM$  for MBS, MBH, and LC Components Based on ARM Component Analysis and IRM Unmixing

Core	Sample age	MBS- $\chi_{ARM}/IRM$ (mm/A)	MBH- $\chi_{ARM}/IRM$ (mm/A)	LC- $\chi_{ARM}/IRM$ (mm/A)
1218A	3.2 Ma	2.48	2.41	2.34
	4.7 Ma	2.16	2.12	2.08
	10.4 Ma	2.12	1.97	2.14
P4-1	77.6 ka	1.25	1.23	2.12
	241.1 ka	1.33	1.20	1.77
	365.9 ka	1.10	1.20	3.08
ARC5-ICE4	0.4 Ma	0.35	0.26	0.54
	1.0 Ma	0.56	0.53	1.21
	1.9 Ma	0.41	0.43	1.46
L07	5.1 ka	0.76	0.81	7.89
	18.1 ka	0.66	0.65	4.56
	35.2 ka	0.68	0.61	3.94

magnetofossil EMs differ mainly in their coercivity distributions and can be related to the MBS and MBH components, respectively (Egli, 2004a). There is no evidence for single-vortex particles in this hole.

For core P4-1, FORC diagrams contain mixed central ridge and vertically extended signals (Figures 5b-4 to 5b-6). Two EMs are defined from the FORC-PCA results (Figures 5b-2 and 5b-3), which explain ~85% of the data variance. The FORC diagram for EM1 contains an obvious central ridge with ~30 mT peak coercivity that extends to ~100 mT and triangular contours that diverge toward  $B_c = 0$  (Figure 5b-2). For EM2, the FORC diagram has a ~5 mT peak coercivity and wide vertical spreading (Figure 5b-3), which is likely to be due to a mixture of vortex state and MD grains (Egli, 2021; Lascu et al., 2018; Roberts et al., 2017, 2018).

For core ARC5-ICE4, mixed central ridge and vertically extended signals are also detected in FORC diagrams (Figures 5c-5 to 5c-7). Three EMs are identified in FORC-PCA results (Figures 5c-2 to 5c-4), which explain ~85% of the data variance. FORC diagrams for EM1 (Figure 5c-2) and EM2 (Figure 5c-3) both contain obvious central ridges and vertical distributions. The  $B_c$  distributions of EM1 and EM2 peak at ~20 and ~40 mT and extend to ~60 and ~80 mT, respectively. The FORC diagram for EM3 has distinct vertical spreading parallel to the  $B_u$  axis with peak  $B_c$  at ~10–15 mT and extended  $B_c$  distributions along the  $B_u = 0$  axis to higher fields (Figure 5c-4).

For core L07, central ridges and vertically spreading contributions are also observed in FORC diagrams (Figures 5d-5 to 5d-7). Three EMs are identified in the FORC-PCA results (Figures 5d-2 to 5d-4). Three EMs explain ~63% of the data variance. FORC diagrams for EM1 (Figure 5d-2) and EM2 (Figure 5d-3) both have distinct central ridges with vertical extensions. The  $B_c$  distribution for EM1 has a peak at ~20 mT and a tail to ~50 mT, and that of EM2 peaks at ~40 mT and extends to ~100–120 mT. Compared to the vertical spread in EM1 and EM2, the non-central ridge feature indicated by triangular contours diverging toward  $B_c = 0$  is more conspicuous in EM3 (Figure 5d-4).

### 3.5. IRM Unmixing

To evaluate the influence of magnetofossil chain structures, IRM unmixing was conducted for representative samples to obtain the IRM of the MBS and MBH components and to calculate  $\chi_{ARM}/IRM$  for biogenic components. IRM unmixing results are shown in Figure 6. Five components, including the LC, MBS, MBH, HC, and hematite (H) components were modelled for the four cores.  $\chi_{ARM}/IRM$  values are listed for MBS, MBH, and LC in Table 1 for the four cores. For MBS and MBH, Hole 1218A has the highest values, and ARC5-ICE4 and L07 have relatively low values.

## 4. Discussion

### 4.1. Hole 1218A

For Eastern Pacific Hole 1218A, a consistent relationship between bulk ARM ( $ARM_{Bulk}$ ) and ARM carried by biogenic components ( $ARM_{MBS+MBH}$ ) is found over the last 11 Ma (Figure 2a-1) with correlation coefficient,  $r = 0.98$  (Figure 2a-3).  $ARM_{Bulk}$  correlates less well with the LC component (Figure 2a-3). A marked LC peak occurs at 3.2 Ma (Figure 2a-2), where a sharp  $ARM_{Bulk}$  drop (Figure 2a-1) may be caused by the lower  $\chi_{ARM}/SIRM$  of this component in this hole (Table 1). The LC peak might be caused by an increased detrital contribution to the LC component, which led to dilution of the magnetofossil signal (e.g., Heslop et al., 2013).

Quantile contours provide an objective measure of vertical spread in FORC diagrams and of the relative central ridge contribution (Egli, 2021). Quantitative analyses of FORC EMs based on quantile contours and coercivity distributions enable deeper interpretation of FORC-PCA results and provide unbiased EM representations. As shown in Figures 7a-1 and 7a-2, the EM1 and EM2 FORC diagrams with quantile contours contain central ridges and negative regions in the lower quadrants, which are typical of uniaxial non-interacting SD (UNISD) particles

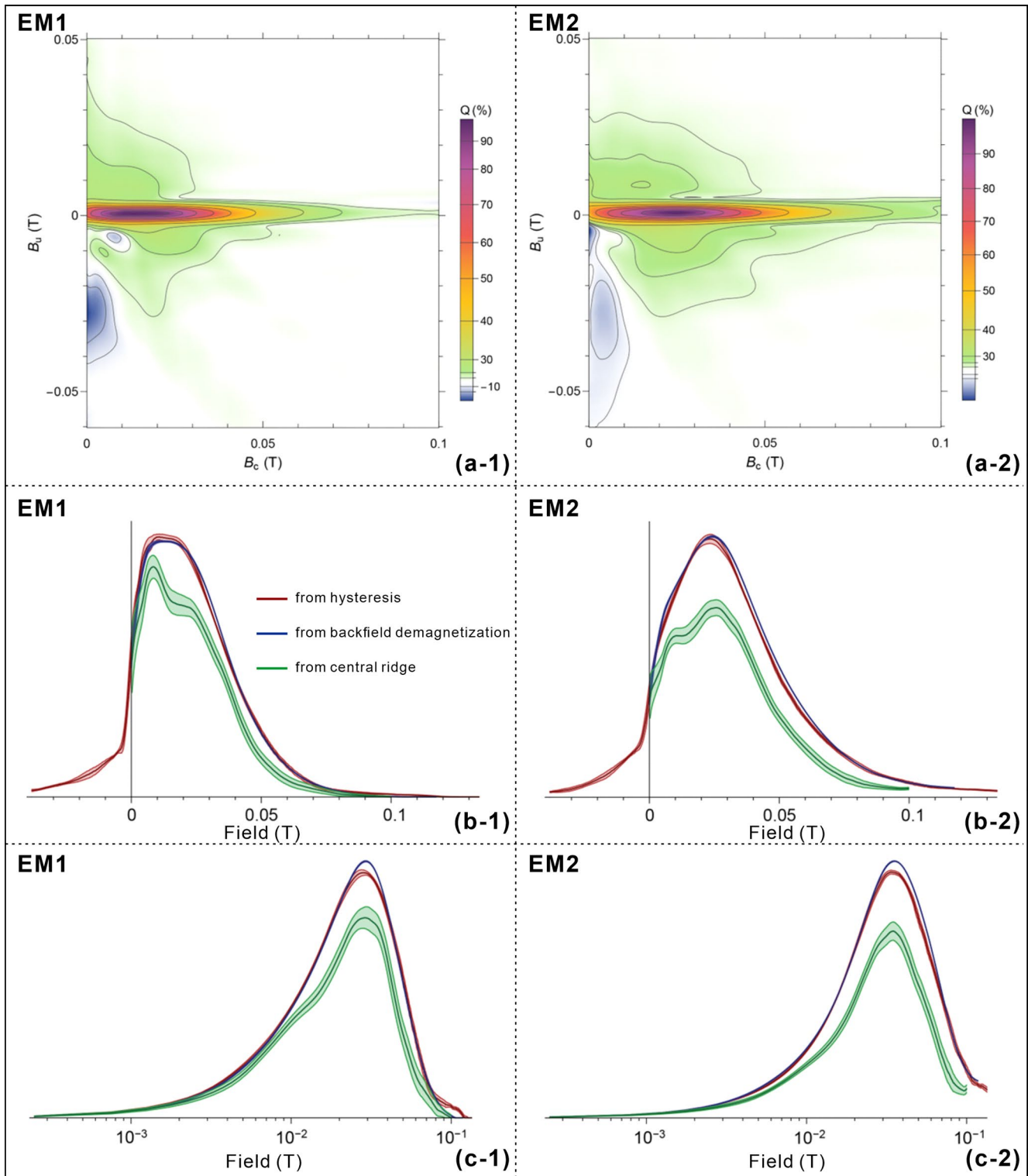


Figure 7.

and magnetofossil chains (Egli et al., 2010; Heslop et al., 2014; Roberts et al., 2012). The central ridges of EM1 and EM2 are surrounded by two asymmetric lobes; the upper one terminates sharply at  $B_c \approx 30$  mT (EM1, the outermost 30% quantile contour in the upper quadrant of Figure 7a-1) and  $\sim 50$  mT (EM2, the outermost 30% quantile contour in the upper quadrant of Figure 7a-2), which are a characteristic signature of multi-stranded

(or fold-collapsed) magnetosome chains (Amor et al., 2022). The lobes around the central ridge are caused by nucleation and annihilation of flux-closure (FC) magnetic states, which can form in multi-stranded (or fold-collapsed) chains, but not in single-stranded ones (Amor et al., 2022; Egli, 2021). Single- and multi-stranded (or fold-collapsed) chains contribute differently to the ARM. For single-stranded chains, ARM represents the room-temperature thermodynamic equilibrium between two symmetric SD states (with all magnetic moments parallel or antiparallel to the chain axis) in a decaying AF, as is the case for UNISD particles (Egli & Lowrie, 2002). Corresponding  $\chi_{ARM}/IRM$  values of 2–3 mm/A (Moskowitz et al., 1993) depend only on the energy barrier of a thermally activated transition between SD states. In multi-stranded (or fold-collapsed) chains, FC states are selected because of their smaller energy, so that the corresponding ARM is associated with the energy barrier of FC denucleation, which is similar to that of FC states in single-stranded chains (Amor et al., 2022). However, because of the small or vanishing magnetic moment of FC states,  $\chi_{ARM}/IRM$  of multi-stranded (or fold-collapsed) chains is considerably smaller (Pan et al., 2005). Multi-stranded (or fold-collapsed) chains also contribute to the BS and BH components, so that lower-than-usual  $\chi_{ARM}/IRM$  values for these components (e.g., Egli, 2004c), can be explained by a higher proportion of multi-stranded (or fold-collapsed) chains.

For Hole 1218A, elevated  $\chi_{ARM}/IRM$  values for biogenic components (MBS and MBH) (Table 1) and good correlation between  $ARM_{Bulk}$  and the EM1 + EM2 magnetizations ( $Mag_{EM1+EM2}$ ) (Figure 8a-3) confirm that magnetofossils (mainly single-stranded chains), control ARM variations. Even so, quantile contours in the EM1 and EM2 FORC diagrams contain distinct multi-stranded (or fold-collapsed) chain signatures, so we try to quantify their fractions as follows. The largest  $\chi_{ARM}/IRM$  values encountered for BS and BH coercivity components are close to 5 mm/A (Egli, 2004a). Multi-stranded chains lower  $\chi_{ARM}/IRM$ , so it can be assumed that a maximum of 5 mm/A corresponds to cases where single-stranded chains are dominant. This value is larger than the 3.4 mm/A average for cultured MTB (see Table 1 in Amor et al. (2022)); however, cultured MTB samples are usually concentrated so that magnetostatic interactions become important. The MBH- $\chi_{ARM}/IRM$  average value of three samples in Hole 1218A is 2.167 mm/A (Table 1). Assuming that multi-stranded (or fold-collapsed) chains do not contribute to the ARM, the maximum relative fraction of single-stranded chains is  $2.167/5 = 43\%$ . Consider now the EM2, where the central ridge contributes  $\sim 64.3\%$  of the total FORC magnetization (the number comes from separating the central ridge and calculating the integral of the separated central ridge (Egli, 2013, 2021)). For comparison, the micromagnetically modelled mean central ridge contributions of single-stranded and multi-stranded (double or fold-collapsed) chains are  $r_{ss} = 93\%$  and  $r_{ms} = 50\%$ , respectively (see Table 3 in Amor et al. (2022)). Assuming  $p$  and  $1 - p$  to be the fractions of single-stranded and multi-stranded (or fold-collapsed) chains, the relative contribution of the central ridge to the total FORC magnetization is given by:

$$\left( \frac{M_{cr}}{M_{forc}} \right)_{mixture} = pr_{ss} + (1 - p)r_{ms}. \quad (3)$$

Solving with respect to  $p$  gives:

$$p = \frac{\left( \frac{M_{cr}}{M_{forc}} \right)_{mixture} - r_{ms}}{r_{ss} - r_{ms}}. \quad (4)$$

The above estimate gives  $p = 33\%$  in the EM2. Hence, two independent single-stranded chain fraction estimates yield consistent values of 43% and 33%. Thus, it can be inferred that the multi-stranded (or fold-collapsed) chain fractions ( $\sim 57$  and 67%) are relatively stable and non-negligible.

The correlation coefficient between  $ARM_{MBH}$  and  $Mag_{EM2}$  ( $r = 0.94$ , Figure 9a-2) is higher than that between  $ARM_{MBS}$  and  $Mag_{EM1}$  ( $r = 0.80$ , Figure 9a-1). For pure magnetofossils, a central maximum in FORC diagrams

**Figure 7.** Quantitative analyses of FORC EMs for Hole 1218A based on quantile contours (a-1 and a-2) and coercivity distributions (b-1, b-2, c-1, c-2). Coercivity distributions plotted on (b-1 and b-2) linear and (c-1 and c-2) logarithmic field scales. The two scales are useful for detecting different features. Depending on coercivity component overlaps, some components are more visible on either a linear or a logarithmic scale. Three coercivity distribution types can be obtained from FORC measurements:  $f_{hys}$  is the derivative of the irreversible component of the ascending hysteresis loop branch (red curves),  $f_{dcd}$  is the derivative of DC (backfield) demagnetization of  $M_{rs}$  (blue curves), and  $f_{cr}$  is the coercivity distribution of the central ridge (green curves). Red curves ( $f_{hys}$ ) over negative fields correspond to non-central ridge features in the FORC diagram upper quadrant. Bulk EM properties can be obtained: EM1:  $M_{rs}/M_s = 0.335$ ,  $M_{cr}/M_{rs} = 0.775$ , and non-central ridge contributions (22.5%) in the upper quadrant are limited to  $B_c = 30$  mT. EM2:  $M_{rs}/M_s = 0.400$ ,  $M_{cr}/M_{rs} = 0.670$ , and non-central ridge contributions (33%) in the upper quadrant are limited to  $B_c = 50$  mT.  $M_{cr}$ ,  $M_s$ , and  $M_{rs}$  are the central ridge magnetization, saturation magnetization, and saturation remanence in magnetization units of the EM components, respectively.

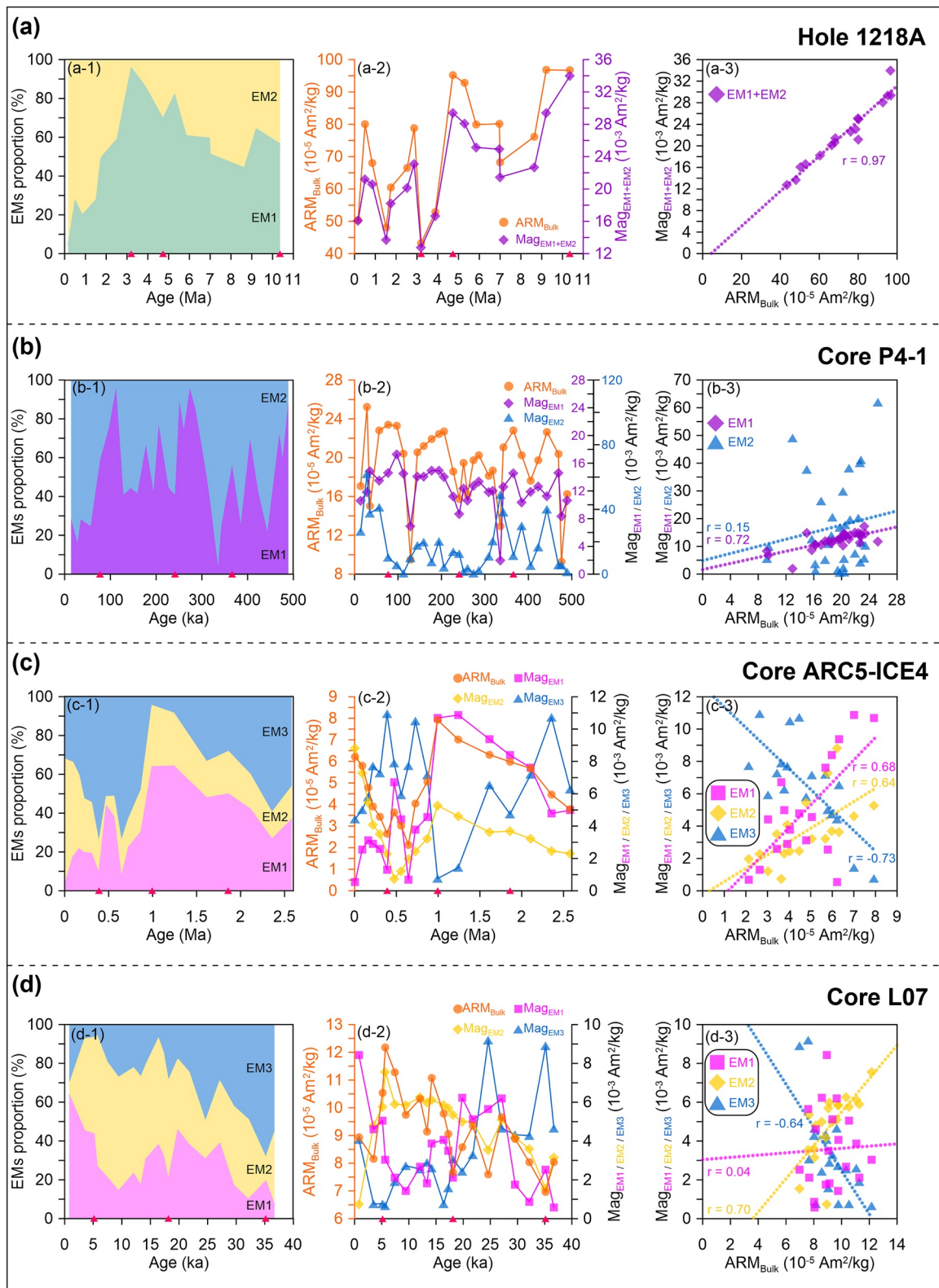


**Figure 8.** Comparison between ARM and FORC-PCA results. (a-1 to d-1) Variations of EM proportions obtained from FORC-PCA. (a-2 to d-2) Variations of ARM<sub>Bulk</sub> and magnetization (Mag) carried by EMs from FORC-PCA. (a-3 to d-3) Correlation diagrams between EM magnetizations and ARM<sub>Bulk</sub>. The correlation coefficient is r. Red triangles on the age axis indicate samples for which FORC diagrams are shown in Figure 5.

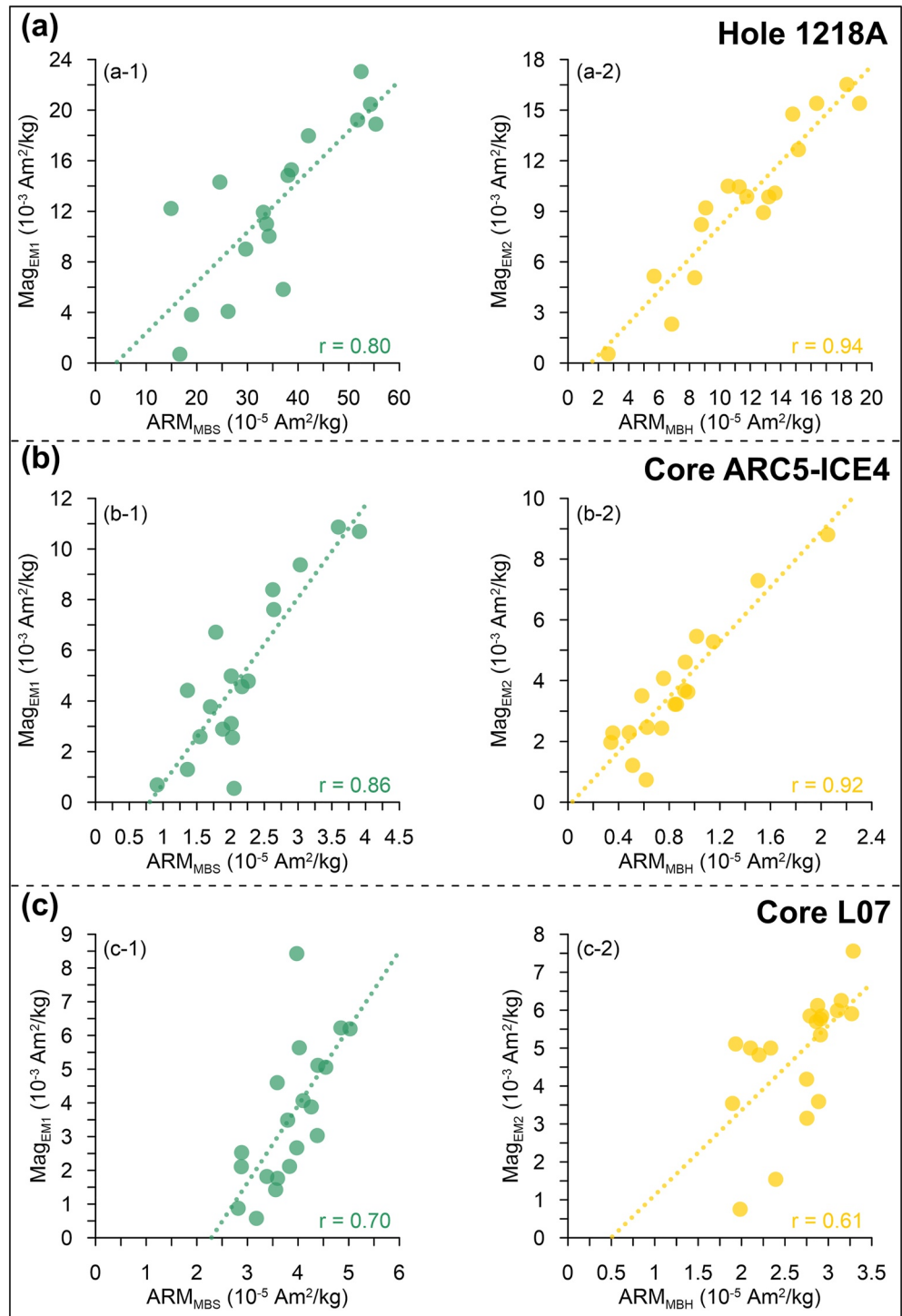


**Figure 9.** Comparison between ARM components and FORC-PCA endmembers. All horizontal axes represent the ARM carried by either MBS or MBH from ARM component analysis. All vertical axes represent the magnetization carried by EMs identified from FORC-PCA. The correlation coefficient is  $r$ .

should be detached from the  $B_c = 0$  axis (Amor et al., 2022; Chang et al., 2019; Ludwig et al., 2013). However, the maximum is close to  $B_c = 0$  in the EM1 central ridge (Figure 5a-2). Hence, some non-magnetofossil SD contributions (i.e., LC components) may be present in EM1. This can be confirmed by quantitative analysis. For example, the FORC contours of both EMs merge with  $B_c = 0$ , which lowers  $M_{rs}/M_s$  below the expected

magnetofossil value. This is also due to central ridge LC contributions. More limitations of FORC-PCA can also be seen in the following case. The EM1 and EM2 central ridge coercivity distributions both contain three components at  $\sim 10$ ,  $\sim 27$ , and  $\sim 50$  mT (green curves, Figures 7c-1 and 7c-2), which correspond to the LC, MBS, and MBH components. This means that FORC-PCA did not separate magnetofossil signatures completely in terms of coercivity, nor in terms of single-vs. multi-stranded (or fold-collapsed) chains. Nevertheless, LC is most pronounced in EM1 (Figure 7c-1) and MBH is most pronounced in EM2 (Figure 7c-2), which indicate that EM2 contains most if not all of the MBH component, while EM1 contains more of the LC component. Incomplete separation of non-central ridge signatures in FORC-PCA results might be because EM1 and EM2 are close to the limits of PC1 variability, and thus to the natural sample variability, which lack cases with only one coercivity component or only one magnetofossil chain type. Pushing EM1 and EM2 further apart in PC space could result in better separation, although choosing EMs that are far from samples in PC space can amplify noise and produce unmixing artifacts.

#### 4.2. Core P4-1

For Antarctic margin core P4-1, magnetofossils contribute most of the  $ARM_{Bulk}$  (Figure 2b-2), which is dominated by  $ARM_{MBS+MBH}$  since 500 ka (Figures 2b-1 and 2b-3). Correlation between  $ARM_{Bulk}$  and  $ARM_{LC}$  is better for core P4-1 than for Hole 1218A, which means that the LC component also contributes to ARM in core P4-1.  $ARM_{Bulk}$  has no clear relationship with  $Mag_{EM2}$  (Figure 8b-3), which means that coarse vortex state (or) MD particles contribute little to ARM variations in this core. EM1 has a marked central ridge (Figure 5b-2), although correlation between  $ARM_{Bulk}$  and  $Mag_{EM1}$  is comparatively poor ( $r = 0.72$ ; Figure 8b-3).  $\chi_{ARM}/IRM$  for the MBS and MBH components for core P4-1 (Table 1) is lower than for single-stranded magnetofossil chains (2–3 mm/A; Moskowitz et al., 1993). Hence, vertical spreading of the non-central ridge contribution in EM1 may be partly caused by multi-stranded (or fold-collapsed) chains, which could be responsible for poor correlation between  $ARM_{Bulk}$  and  $Mag_{EM1}$  (Figure 8b-3).

Constraints on FORC EM and ARM interpretations can be further obtained from quantile contour and coercivity distribution analysis. A central ridge and negative region in the lower quadrant are evident from FORC quantile contours for EM1 (Figure 10a-1), which is typical of single-stranded magnetofossil chains. The positive bulge in the lower quadrant at  $B_c = 100$  mT is not typical of magnetofossils and might be an unmixing artifact, or part of a HC contribution (e.g., Roberts et al., 2021). The EM1 backfield coercivity distribution is bimodal with peaks at  $\sim 45$  and  $\sim 100$  mT (blue curves, Figure 10c-1). The  $\sim 45$  mT peak represents the main central ridge magnetofossil contribution. The other peak at  $\sim 100$  mT may indicate the HC contribution. Overall, EM1 contains overlapping magnetofossil and lithogenic signatures. EM2 contains a minor central ridge contribution, especially in the LC range (up to  $\sim 20$  mT, Figure 10a-2). A central ridge tail extending to  $>100$  mT might be associated with a BH contribution. EM2 also contains a vertical ridge and triangular contours in the  $B_c < 20$  mT range, which are typical of large vortex state to MD particles. This contribution is absent in EM1. The low  $M_{rs}/M_s$  of EM2 is due to the lack of a major central ridge contribution and the presence of a MD signature. The backfield coercivity distribution of EM2 is apparently unimodal with a main peak at  $\sim 100$  mT (blue curves, Figure 10c-2), which reflects the main HC contribution. On a linear scale, this includes a LC component (Figure 10b-2), which is associated with large vortex state to MD particles. A small central ridge contribution is mainly concentrated in the LC range ( $B_c < 20$  mT), which is also the  $B_c$  range of the MD FORC signature. The sharp LC central ridge termination is unnatural (green curves, Figure 10b-2) because the LC component (Egli, 2004a) is characterized by progressive decay to  $B_c \approx 100$  mT. Therefore, this termination is likely associated with imperfect central ridge isolation due to low measurement resolution and the large smoothing needed to suppress noise. This interpretation is supported by the fact that the central ridge is offset upward for  $B_c < 20$  mT, with an abrupt width decrease at  $B_c \approx 20$  mT. Central ridges are usually offset upward due to thermally activated switching (Berndt et al., 2018; Pike et al., 2001).

Overall, FORC-PCA results partially separate biogenic (EM1) and lithogenic (EM2) components in core P4-1. Traces of a lithogenic component are present in EM1, and traces of a magnetofossil component are present in EM2. This incomplete separation and the influence of multi-stranded (or fold-collapsed) chains may contribute to the lower positive correlation between  $ARM_{Bulk}$  and  $Mag_{EM1}$  (Figure 8b-3). Incomplete FORC-PCA separation of magnetofossil and lithogenic components might be related to the fact that EM1 and EM2 lie relatively close to each other in PC space. Both endmembers also contain unmixing artifacts, so that selecting EMs that are further

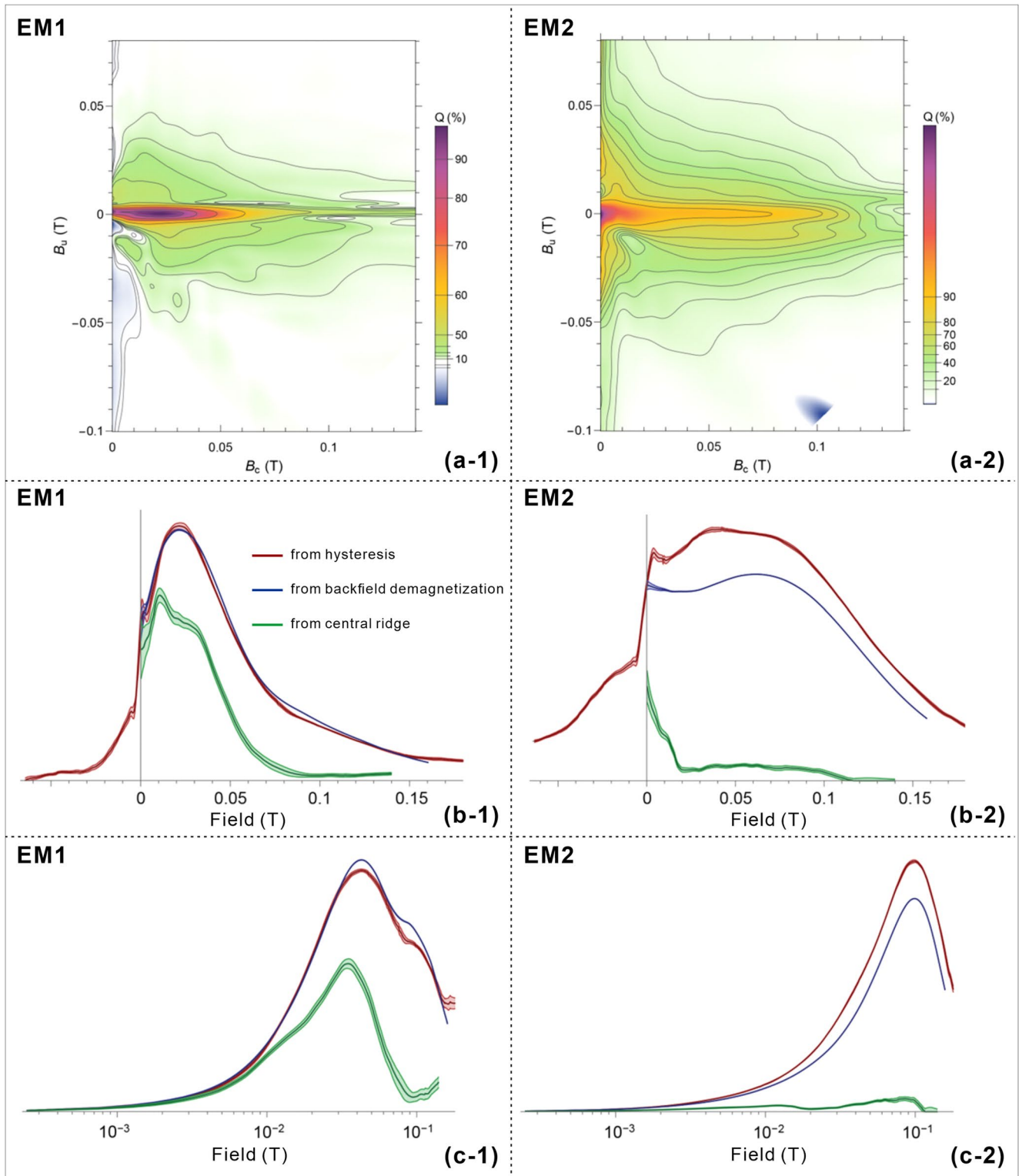


**Figure 10.** Quantitative FORC EM analyses for core P4-1 based on quantile contours (a-1 and a-2) and coercivity distributions (b-1, b-2, c-1, c-2). Coercivity distributions plotted on a (b-1 and b-2) linear field scale and (c-1 and c-2) logarithmic field scale. Bulk EM properties can be obtained: EM1:  $M_{rs}/M_s = 0.356$ ,  $M_{cr}/M_{rs} = 0.471$ , and non-central ridge contributions (52.9%) are only slightly asymmetric and reflect the central ridge coercivity distribution. EM2:  $M_{rs}/M_s = 0.224$ ,  $M_{cr}/M_{rs} = 0.072$ , and non-central ridge contributions (92.8%) dominate with a significant HC fraction.

apart in PC space would exacerbate this issue. Unmixing artifacts are likely due to the fact that part of the sample variability is not described by PC1.

### 4.3. Core ARC5-ICE4

For Arctic Ocean core ARC5-ICE4, correlation coefficients between the biogenic/low-coercivity components and  $ARM_{Bulk}$  are both high (Figure 2c-3). This reflects considerable magnetofossil and LC (i.e., mixed D + EX) contributions to ARM. Although EM1 and EM2 (Figures 5c-2 and 5c-3) have similar  $B_c$  distributions to those from Hole 1218A (Figures 5a-2 and 5a-3), non-central ridge contributions in EM1/EM2 for core ARC5-ICE4 have vertical spreading, which means that the two EMs cannot be interpreted as simply as for Hole 1218A. Low amplitude FORC contours tend to be oval for pure magnetofossil components (Amor et al., 2022; Chang et al., 2019; Ludwig et al., 2013) and triangular for vortex state particles (Lascu et al., 2018). The EM1 and EM2 coercivity distributions, with maxima close to  $B_c = 0$ , are not typical magnetofossil features (Figures 5c-2 and 5c-3). Hence, non-magnetofossil contributions are likely present in EM1 and EM2.  $\chi_{ARM}/IRM$  for MBS and MBH in core ARC5-ICE4 is much smaller than for single-stranded magnetofossil chains (Table 1), which implies that multi-stranded (or fold-collapsed) chains may contribute significantly to the biogenic components. Further information is evident from the quantitative FORC EM analyses below.

All EMs with quantile contours contain central ridges in core ARC5-ICE4 (Figures 11a-1 to 11a-3). Non-central ridge EM2 contributions are slightly asymmetric (Figure 11a-2), with 30% and 40% quantile contours indicating the sharp termination expected for magnetofossils (Amor et al., 2022). In the lower quadrant, EM1 contains features along the descending diagonal (Figure 11a-1), which include negative amplitudes, which are often associated with vortex state and MD particles (Egli, 2021). The backfield coercivity distribution for EM1 is bimodal with peaks at  $\sim 50$  and  $\sim 100$  mT (blue curves, Figure 11c-1), while the central ridge coercivity distribution features three distinct peaks at  $\sim 10$ ,  $\sim 40$ , and  $> 120$  mT (green curves, Figure 11c-1). The latter peaks are apparently associated with narrow coercivity distributions. The sharp LC component termination at  $\sim 20$  mT is unnatural (green curves, Figure 11b-1) because such a component is expected to decay exponentially to  $\sim 100$  mT (Egli, 2004a). Therefore, sharp separation of the three central ridge peaks must be due partially to unmixing artifacts. Overall, EM1 has mixed features expected for biogenic and lithogenic particles, which is consistent with our interpretations above. EM2 (Figure 11a-2) contains typical magnetofossil signatures described by Amor et al. (2022), including asymmetric non-central ridge contributions with a sharp upper quadrant termination. Unlike micromagnetic simulations of single- and multi-stranded (or fold-collapsed) chains, the EM2 FORC contours intersect the  $B_c = 0$  limit. This is also due to a LC component. The EM2 backfield coercivity distribution is unimodal and skewed (blue curves, Figure 11c-2). These properties are shared by the central ridge distribution, with a main peak at  $\sim 45$  mT (green curves, Figure 11c-2). FORC contours for EM3 (Figure 11a-3) converge gradually to the central ridge in the high-coercivity range, with contributions beyond  $\sim 150$  mT. These characteristics are similar to those of silicate-hosted magnetic minerals (Chang, Roberts, et al., 2016). The EM3 backfield coercivity distribution is bimodal with peaks at  $\sim 30$  and  $\sim 90$  mT (blue curves, Figure 11c-3), and a pronounced HC contribution. The central ridge contribution ends abruptly at  $\sim 75$  mT (green curves, Figure 11c-3) and is likely affected by noise or unmixing artifacts. Nevertheless, the lack of HC contributions indicates that the central ridge and remaining contributions have a different origin.

In summary, magnetofossil signatures are visible in EM1, but are unclear due to overlap with lithogenic signals. The magnetofossil component is mainly captured by EM2 along with a LC component. These are likely responsible for the worse correlation between  $Mag_{EM1}$  and  $ARM_{MBS}$  (Figure 9b-1) than between  $Mag_{EM2}$  and  $ARM_{MBH}$  (Figure 9b-2). This incomplete separation also leads to the less positive relationships between  $Mag_{EM1}/Mag_{EM2}$  and  $ARM_{Bulk}$  (Figure 8c-3). The EM3 FORC signature appears to be the sum of LC and HC lithogenic contributions, and is probably a mixture of fine-grained silicate-hosted magnetic minerals (Chang, Roberts, et al., 2016) and larger vortex state to MD particles. Vortex state to MD (titano)magnetite has been reported in core ARC5-ICE4 sediments (Liu et al., 2019). The lithogenic origin of EM3 is also confirmed by its negative correlation with  $ARM_{Bulk}$  (Figure 8c-3). Abundant coarse (titano)magnetite might have a strong diluting effect (Heslop et al., 2013) that lowers  $ARM_{Bulk}$ . Incomplete lithogenic and biogenic separation in this core might be caused by unmixing artifacts due to the large distance of EMs from the PC region covered by the samples (Figure 5c-1), which amplifies small FORC variations. The data scatter suggests no distinct mixing triangle, which can lead to arbitrary EM placement in PC space (Figure 5c-1). Furthermore, EMs might not be fixed over

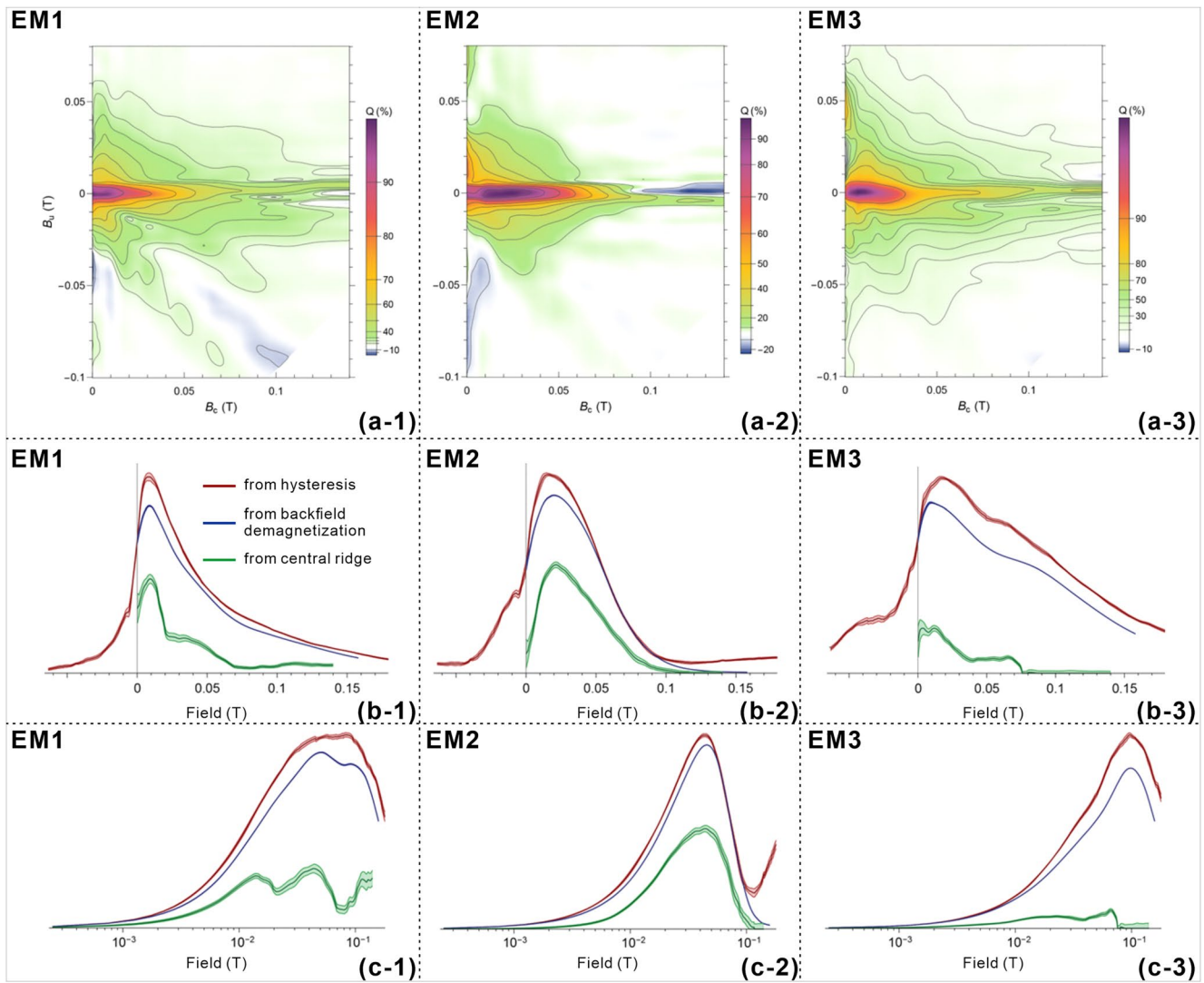


**Figure 11.** Quantitative analyses of FORC EMs for core ARC5-ICE4 based on quantile contours (a-1, a-2, and a-3) and coercivity distributions (b-1, b-2, b-3, c-1, c-2, c-3). Coercivity distributions plotted on (b-1, b-2, and b-3) linear and (c-1, c-2, and c-3) logarithmic field scales. Bulk EM properties can be obtained: EM1:  $M_{rs}/M_s = 0.286$ ,  $M_{cr}/M_{rs} = 0.327$ , and non-central ridge contributions (67.3%, noisy). EM2:  $M_{rs}/M_s = 0.290$ ,  $M_{cr}/M_{rs} = 0.486$ , and non-central ridge contributions (51.4%) are asymmetric with upper quadrant termination at  $\sim 55$  mT, similar to the magnetofossil signature calculated by Amor et al. (2022), with unmixing artifact along the central ridge above 100 mT. EM3:  $M_{rs}/M_s = 0.225$ ,  $M_{cr}/M_{rs} = 0.111$ , and non-central ridge contributions (88.9%) over the upper and lower quadrant are nearly symmetric.

time, as suggested by the two linear trends over the positive PC1 range (Figure 5c-1). Adding more EMs would add noise and unmixing artifacts. The separated EMs are obviously contaminated for core ARC5-ICE4, which is a limitation of the FORC-PCA approach.

#### 4.4. Core L07

For South China Sea core L07, the correlation coefficient between  $ARM_{Bulk}$  and  $ARM_{MBS+MBH}$  (Figure 2d-3) is lower than those for the other three cores (Figures 2a-3, 2b-3, and 2c-3). This may be related to the HC component, which is larger in core L07 (Figures 3d-2 to 3d-4). Regardless, the magnetofossil and LC components both contribute significantly to ARM variations in this core (Figure 2d-2).  $ARM_{Bulk}$  and  $Mag_{EM1}/Mag_{EM2}$  (Figure 8d-3),  $ARM_{MBS}$  and  $Mag_{EM1}$  (Figure 9c-1), and  $ARM_{MBH}$  and  $Mag_{EM2}$  (Figure 9c-2), all correlate relatively poorly, which reflects the complexity of EM representation for core L07. Quantitative FORC EM analysis provides better insight into this issue.

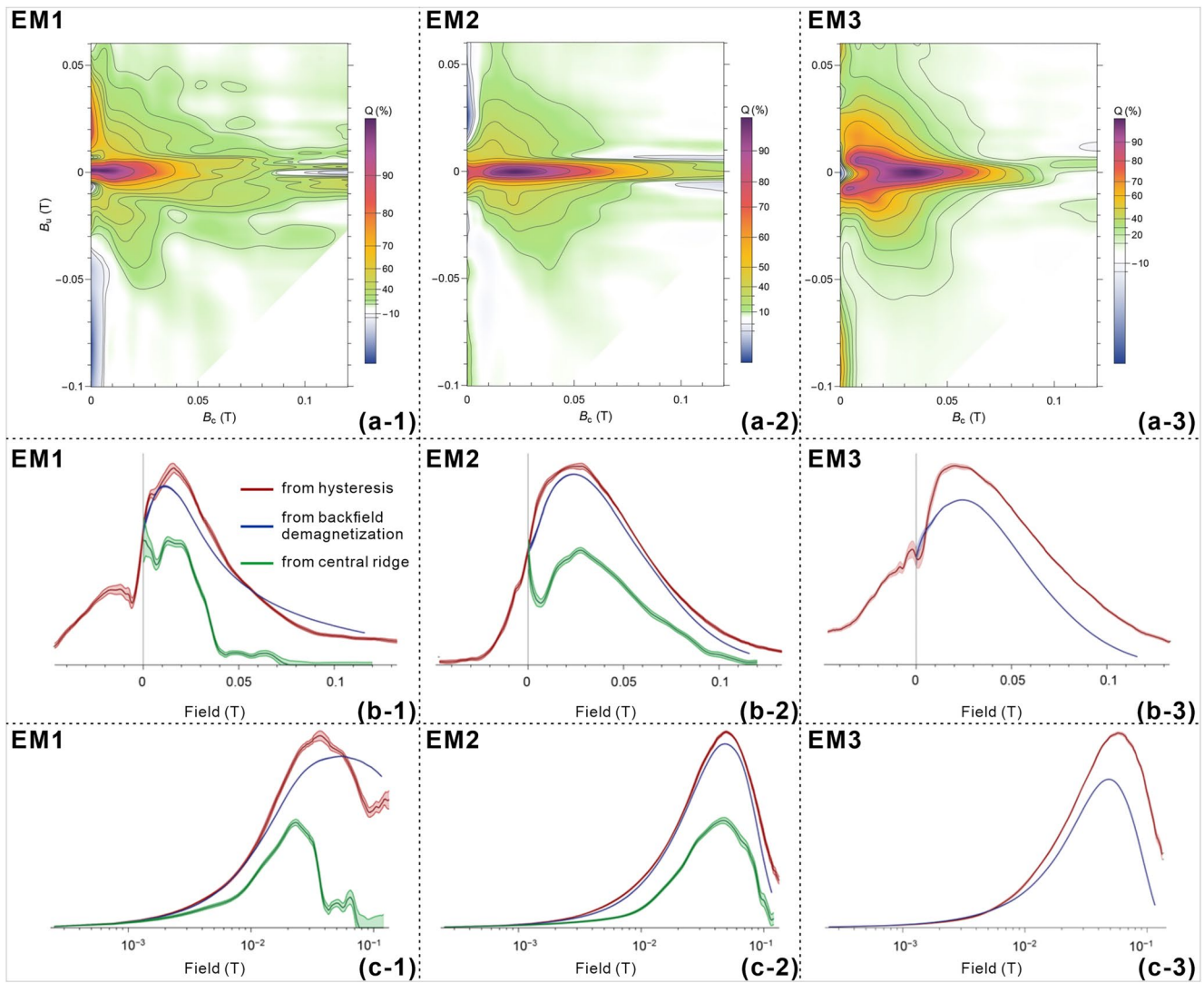


**Figure 12.** Quantitative analyses of FORC EMs for core L07 based on quantile contours (a-1, a-2, and a-3) and coercivity distributions (b-1, b-2, b-3, c-1, c-2, c-3). Coercivity distributions plotted on (b-1, b-2, and b-3) linear and (c-1, c-2, and c-3) logarithmic field scales. Bulk EM properties can be obtained: EM1:  $M_r/M_s = 0.286$ ,  $M_c/M_s = 0.328$ , and non-central ridge contributions (67.2%; noisy and affected by unmixing artifacts). EM2:  $M_r/M_s = 0.324$ ,  $M_c/M_s = 0.543$ , and non-central ridge contributions (45.7%; noisy and affected by slight unmixing artifacts). EM3:  $M_r/M_s = 0.197$ ,  $M_c/M_s = 0$ , and unmixing artifact near the origin.

Interpretation of EM1 (Figure 12a-1) is difficult because of noise and unmixing artifacts (e.g., the positive vertical “ridge” in the upper quadrant and its negative counterpart in the lower quadrant are the complements of vertical ridges in EM2 and EM3). Furthermore, large negative field contributions to the coercivity distribution obtained from hysteresis reflect significant lithogenic contributions to EM1 (red curves, Figure 12b-1). The EM1 backfield coercivity distribution is bimodal, with two components at  $\sim 50$  and  $\sim 100$  mT to form a broad maximum (blue curves, Figure 12c-1). In contrast, the central ridge coercivity distribution terminates sharply and unnaturally at  $\sim 45$  mT (green curves, Figure 12c-1). This confirms the noise and unmixing artifacts associated with EM1, which are further revealed by the lack of correlation between  $\text{Mag}_{\text{EM1}}$  and  $\text{ARM}_{\text{Bulk}}$  (Figure 8d-3). EM2 (Figure 12a-2) has a typical magnetofossil signature with strong non-central ridge contributions (45.7%, compared to 22.5%–33% in EM1 and EM2 of Hole 1218A), which are consistent with micromagnetic simulations of multi-stranded (or fold-collapsed) chains (Amor et al., 2022). Low  $\chi_{\text{ARM}}/\text{IRM}$  values in core L07 further confirm this conclusion (Table 1). EM3 (Figure 12a-3), on the other hand, contains typical vortex state signals, apart from an unmixing artifact near the origin, which splits the central peak. The EM2 and EM3 backfield coercivity distributions are unimodal and peak at  $\sim 50$  mT (blue curves, Figures 12c-2 and 12c-3); however, the magnetic particles that produce these distributions are completely different. The coercivity distribution for

EM2 is due to magnetofossils, while for EM3 it is due to single vortex magnetite. The significant lithogenic contribution to EM3 is indicated by the large hysteresis coercivity distribution at negative fields (red curves, Figure 12b-3). Core L07 is located in the northwestern South China Sea sub-basin, where the main sediment source is the Pearl River (Clift et al., 2002; Li et al., 2003; Wan et al., 2007). Hence, the negative correlation between  $ARM_{Bulk}$  and  $Mag_{EM3}$  (Figure 8d-3) can be attributed speculatively to fluvial dilution of the in situ magnetofossil signal. Furthermore, the oval-shaped FORC data cluster in PC1-PC2 space (Figure 5d-1) means that the vertices of the triangle defined by EM1 to EM3 are poorly constrained, as are the EM characteristics. Thus, the empirically obtained EMs are probably linear combinations of physical EMs, with magnetofossil EMs containing detrital contributions. Therefore, lack of complete separation of biogenic and lithogenic contributions leads to the poor correlations discussed (Figures 8d-3, 9c-1, and 9c-2).

#### 4.5. Limitations of FORC-PCA

Incomplete component separations in the FORC-PCA results discussed here, especially for cores ARC5-ICE4 and L07, reveal the limitations of FORC-PCA for natural samples. These limitations are evident as: (a) difficulty in unmixing magnetofossil components with significant contributions from multi-stranded (or fold-collapsed) chains, where non-central ridge contributions lack fixed characteristics; (b) poorly conditioned unmixing, with individual samples dispersed in PC space (e.g., cores ARC5-ICE4 and L07), which contributes to poor definition of the polygon spanned by EMs, and thus the EM characteristics; (c) noise amplification due to extrapolation of measurements over PC regions that are far from measured data, and (d) violation of the assumption of PCA that FORC results are linear combinations of a fixed set of invariable PCs. Biogenic and lithogenic components might be affected by natural variations that require additional, small-amplitude PCs. Adding PCs creates two main problems: they also capture measurement noise, and define additional EMs with no physical meaning.

Quantitative FORC-PCA EM analyses based on quantile contours and coercivity distributions are extremely useful for interpreting FORC-PCA results. Valuable insights are obtained on the nature of PCA endmembers and about unmixing artifacts, which otherwise go undetected in FORC-PCA studies. Stratigraphic or sedimentological information may be helpful for constraining the limitations of FORC-PCA results. All of these quantitative analyses are conducive to improving ARM data interpretation in marine sediments.

#### 4.6. Discussion of ARM Carriers

Magnetofossils are the dominant ARM carrier in the four studied sediment cores. For quantitative ARM interpretation, let us formulate the contributions from different components as follows:

$$\chi_{ARM} = M_{mf} \chi_{mf} + M_{sd} \chi_{sd} + M_{nsd} \chi_{nsd}, \quad (5)$$

where  $\chi_{ARM}$  is the bulk ARM susceptibility,  $M_i$  is the saturation remanence of component “i” with “mf” = magnetofossils, “sd” = non-magnetofossil SD particles (e.g., silicate inclusions or pedogenic magnetite), “nsd” = non-SD particles (e.g., vortex state, not associated with multi-stranded (or fold-collapsed) magnetofossil chains), and  $\chi_i = (\chi_{ARM} / M_{rs})_i$  is the ARM ratio of component “i”. As discussed by Amor et al. (2022),  $\chi_{mf}$  of single-stranded chains corresponds to the value expected for UNISD particles (Egli & Lowrie, 2002). The same is true for  $\chi_{sd}$  if particles are non-interacting, as appears to be the case for pedogenic magnetite (Egli, 2004a, 2021), which can enter the sediment pool as a detrital component. A component similar to pedogenic magnetite can also be produced by bacteria (i.e., extracellular magnetite) through biologically induced mineralization where bacteria modify their local extracellular environment to create chemical conditions suitable for magnetite precipitation (Moskowitz et al., 1993). There is no strict biological control over particle synthesis, so extracellular magnetite has broad grain size distributions and rounded shapes (Sparks et al., 1990). Finally,  $\chi_{nsd}$  is controlled strongly by grain size. Magnetostatic interactions and grain size variations affect the ARM, so we can rewrite Equation 5 in a more practical form:

$$\chi_{ARM} = M_{unisd} \chi_{unisd} + M_{rest} \chi_{rest}, \quad (6)$$

where the subscript “unisd” refers to UNISD particles and systems of SD particles with two SD-like stable states (Egli et al., 2010), and “rest” puts all remaining contributions together.  $\chi_{unisd}$  is a nearly fixed quantity determined

by the thermodynamic equilibrium between two magnetic states (Egli & Lowrie, 2002), while  $\chi_{rest}$  is affected by several non-quantifiable parameters. If  $p_{unisd} = M_{unisd} / M_{rs}$  is the relative fraction of UNISD particles in terms of contributions to the saturation remanence, it can be obtained easily from IRM unmixing. In this case, Equation 6 becomes:

$$\chi_{ARM} = M_{rs} p_{unisd} \chi_{unisd} + M_{rs} (1 - p_{unisd}) \chi_{rest}. \quad (7)$$

In the limit case where  $p_{unisd} \chi_{unisd} \gg (1 - p_{unisd}) \chi_{rest}$ , ARM is proportional to the UNISD component. In all other cases, ARM is not a pure proxy for a magnetic component. The above condition can be rewritten as  $p_{unisd} \gg \chi_{rest} / (\chi_{unisd} + \chi_{rest})$ .  $\chi_{rest}$  is typically about one order or magnitude smaller than  $\chi_{unisd}$  (Egli, 2004a), so ARM is a direct proxy of the UNISD component as long as  $p_{unisd} \gg 0.1$ . For the four studied magnetofossil-rich sediment cores, the relative contributions of biogenic components (MBS and MBH) are much larger than 10% (Figure 6). Hence, the dominance of magnetofossils as the main ARM carrier in the studied sediments is confirmed by the above formulations.

Sediments contain mixtures of magnetic particles with different primary (e.g., lithogenic magnetite-bearing minerals; Chang, Roberts, et al., 2016; Vali et al., 1989) and secondary origins (e.g., diagenetic processes and biomineralization; Fortin & Langley, 2005; Franke et al., 2007; Just et al., 2012; Lovley et al., 1987; Miot et al., 2009; Oldfield, 2007). All examples presented here contain significant non-interacting SD particle contents, isolated or as magnetofossil chains, which permit identification of ARM<sub>Bulk</sub> variations with corresponding ARM components and FORC endmembers. This is because of the extremely high selectivity of ARM to non-interacting SD particles. Magnetofossil dominance is a special case that will not apply when non-SD or interacting SD particles are the main remanence carriers. When non-SD particles dominate, ARM will be grain-size dependent. Even so, our results associate ARM variations with FORC-PCA endmembers for the first time, similar to that done for coercivity components (Egli, 2004a), which provides detailed information about sedimentary ARM carriers. The integrated approach presented here should help to clarify ARM interpretations in future studies.

## 5. Conclusions

We analyzed marine sediments from the Eastern Pacific Ocean, the Antarctic margin, the Arctic Ocean, and the South China Sea. The sampling locations span polar to tropical regions, continental margin to pelagic environments, and timescales of up to millions of years. We analyzed bulk magnetic properties and microscopic features of magnetic minerals using ARM component analysis, FORC-PCA, TEM observations, and IRM unmixing. Bulk ARM variations are evidently controlled mainly by the biogenic magnetite abundance in the four sediment cores studied here — both on long tectonic and shorter orbital timescales. Low coercivity particles (detrital and fine-grained extracellular magnetite) also contribute to ARM variations. Our results indicate that magnetofossil chain structure has a significant influence on ARM interpretation. Quantitative FORC-PCA endmember analyses based on quantile contours and coercivity distributions provide valuable information on the nature of endmembers and aid ARM interpretation.

## Data Availability Statement

The data presented in this paper have been uploaded to the Mendeley Data repository (<http://dx.doi.org/10.17632/2khtrkdfgp.1>).

## References

- Amor, M., Wan, J., Egli, R., Carlut, J., Gatel, C., Andersen, I. M., et al. (2022). Key signatures of magnetofossils elucidated by mutant magnetotactic bacteria and micromagnetic calculations. *Journal of Geophysical Research: Solid Earth*, 127, e2021JB023239. <https://doi.org/10.1029/2021JB023239>
- Arnold, E., Leinen, M., & King, J. (1995). Palaeoenvironmental variation based on the mineralogy and rock magnetic properties of sediment from Sites 885 and 886. *Proceedings of the Ocean Drilling Program: Scientific Results*, 145, 231–245.
- Banerjee, S. K., King, J., & Marvin, J. (1981). A rapid method for magnetic granulometry with applications to environmental studies. *Geophysical Research Letters*, 8(4), 333–336. <https://doi.org/10.1029/GL008i004p00333>
- Bazylinski, D. A., & Frankel, R. B. (2004). Magnetosome formation in prokaryotes. *Nature Reviews Microbiology*, 2(3), 217–230. <https://doi.org/10.1038/nrmicro842>
- Berndt, T. A., Chang, L., & Pei, Z. (2020). Mind the gap: Towards a biogenic magnetite palaeoenvironmental proxy through an extensive finite-element micromagnetic simulation. *Earth and Planetary Science Letters*, 532, 116010. <https://doi.org/10.1016/j.epsl.2019.116010>

## Acknowledgments

The authors thank Prof. Rixiang Zhu for support, the Associate Editor, Agnes Kontny, and Ramon Egli and Tilo von Dobeneck for insightful reviews that helped to improve the paper, and Tingwei Zhang for assistance. This work was supported financially by the Project on the Impact and Response of Antarctic Seas to Climate Change (IRASCC2020-2022-No.01-03-02, No.03-02), Chinese Arctic and Antarctic Administration, the National Natural Science Foundation of China (41876070, 42104076, 41920104009), the China National Postdoctoral Program for Innovative Talents (BX20200332), the China Postdoctoral Science Foundation (2020M680026) for fellowship funding, the Australian Research Council (grant DP200100765), and the Shenzhen Science and Technology Program (KQTD20170810111725321). The International Ocean Discovery Program provided the samples studied here.

- Berndt, T. A., Chang, L., Wang, S., & Badojo, S. (2018). Time-asymmetric FORC diagrams: A new protocol for visualizing thermal fluctuations and distinguishing magnetic mineral mixtures. *Geochemistry, Geophysics, Geosystems*, *19*(9), 3056–3070. <https://doi.org/10.1029/2018GC007669>
- Chang, L., Harrison, R. J., & Berndt, T. A. (2019). Micromagnetic simulation of magnetofossils with realistic size and shape distributions: Linking magnetic proxies with nanoscale observations and implications for magnetofossil identification. *Earth and Planetary Science Letters*, *527*, 115790. <https://doi.org/10.1016/j.epsl.2019.115790>
- Chang, L., Harrison, R. J., Zeng, F., Berndt, T. A., Roberts, A. P., Heslop, D., & Zhao, X. (2018). Coupled microbial bloom and oxygenation decline recorded by magnetofossils during the Palaeocene–Eocene Thermal Maximum. *Nature Communications*, *9*(1), 1–9. <https://doi.org/10.1038/s41467-018-06472-y>
- Chang, L., Heslop, D., Roberts, A. P., Rey, D., & Mohamed, K. J. (2016). Discrimination of biogenic and detrital magnetite through a double Verwey transition temperature. *Journal of Geophysical Research: Solid Earth*, *121*(1), 3–14. <https://doi.org/10.1002/2015JB012485>
- Chang, L., Roberts, A. P., Heslop, D., Hayashida, A., Li, J., Zhao, X., et al. (2016). Widespread occurrence of silicate-hosted magnetic mineral inclusions in marine sediments and their contribution to paleomagnetic recording. *Journal of Geophysical Research: Solid Earth*, *121*(12), 8415–8431. <https://doi.org/10.1002/2016JB013109>
- Chang, L., Roberts, A. P., Williams, W., Fitz Gerald, J. D., Larrasoana, J. C., Jovane, L., & Muxworthy, A. R. (2012). Giant magnetofossils and hyperthermal events. *Earth and Planetary Science Letters*, *351*, 258–269. <https://doi.org/10.1016/j.epsl.2012.07.031>
- Channell, J. E. T., Harrison, R. J., Lascu, I., McCave, I. N., Hibbert, F. D., & Austin, W. E. (2016). Magnetic record of deglaciation using FORC-PCA, sortable-silt grain size, and magnetic excursion at 26 ka, from the Rockall Trough (NE Atlantic). *Geochemistry, Geophysics, Geosystems*, *17*(5), 1823–1841. <https://doi.org/10.1002/2016GC006300>
- Channell, J. E. T., Hodell, D. A., Crowhurst, S. J., Skinner, L. C., & Muscheler, R. (2018). Relative paleointensity (RPI) in the latest Pleistocene (10–45 ka) and implications for deglacial atmospheric radiocarbon. *Quaternary Science Reviews*, *191*, 57–72. <https://doi.org/10.1016/j.quascirev.2018.05.007>
- Channell, J. E. T., Ohneiser, C., Yamamoto, Y., & Kesler, M. S. (2013). Oligocene-Miocene magnetic stratigraphy carried by biogenic magnetite at sites U1334 and U1335 (equatorial Pacific Ocean). *Geochemistry, Geophysics, Geosystems*, *14*(2), 265–282. <https://doi.org/10.1029/2012GC004429>
- Channell, J. E. T., Wright, J. D., Mazaud, A., & Stoner, J. S. (2014). Age through tandem correlation of Quaternary relative paleointensity (RPI) and oxygen isotope data at IODP Site U1306 (Eirik Drift, SW Greenland). *Quaternary Science Reviews*, *88*, 135–146. <https://doi.org/10.1016/j.quascirev.2014.01.022>
- Chen, L., Heslop, D., Roberts, A. P., Chang, L., Zhao, X., McGregor, H. V., et al. (2017). Remanence acquisition efficiency in biogenic and detrital magnetite and recording of geomagnetic paleointensity. *Geochemistry, Geophysics, Geosystems*, *18*(4), 1435–1450. <https://doi.org/10.1002/2016GC006753>
- Clift, P., Lee, J. I., Clark, M. K., & Blusztajn, J. (2002). Erosional response of South China to arc rifting and monsoonal strengthening; A record from the South China Sea. *Marine Geology*, *184*, 207–226. [https://doi.org/10.1016/S0025-3227\(01\)00301-2](https://doi.org/10.1016/S0025-3227(01)00301-2)
- Coakley, B., Brumley, K., Lebedeva-Ivanova, N., & Mosher, D. (2016). Exploring the geology of the central Arctic Ocean; Understanding the basin features in place and time. *Journal of the Geological Society*, *173*(6), 967–987. <https://doi.org/10.1144/jgs2016-082>
- Dunlop, D. J., & Özdemir, Ö. (1997). *Rock Magnetism: Fundamentals and frontiers*. Cambridge University Press. <https://doi.org/10.1017/CBO9780511612794>
- Egli, R. (2003). Analysis of the field dependence of remanent magnetization curves. *Journal of Geophysical Research*, *108*(B2). <https://doi.org/10.1029/2002JB002023>
- Egli, R. (2004a). Characterization of individual rock magnetic components by analysis of remanence curves. 1. Unmixing natural sediments. *Studia Geophysica et Geodaetica*, *48*(2), 391–446. <https://doi.org/10.1023/B:SGEG.0000020839.45304.6d>
- Egli, R. (2004b). Characterization of individual rock magnetic components by analysis of remanence curves. 2. Fundamental properties of coercivity distributions. *Physics and Chemistry of the Earth, Parts A/B/C*, *29*, 851–867. <https://doi.org/10.1016/j.pce.2004.04.001>
- Egli, R. (2004c). Characterization of individual rock magnetic components by analysis of remanence curves. 3. Bacterial magnetite and natural processes in lakes. *Physics and Chemistry of the Earth, Parts A/B/C*, *29*, 869–884. <https://doi.org/10.1016/j.pce.2004.03.010>
- Egli, R. (2013). VARIFORC: An optimized protocol for calculating non-regular first-order reversal curve (FORC) diagrams. *Global and Planetary Change*, *110*, 302–320. <https://doi.org/10.1016/j.gloplacha.2013.08.003>
- Egli, R. (2021). Magnetic characterization of geologic materials with first-order reversal curves. In *Magnetic measurement techniques for materials characterization* (pp. 455–604). Springer. [https://doi.org/10.1007/978-3-030-70443-8\\_17](https://doi.org/10.1007/978-3-030-70443-8_17)
- Egli, R., Chen, A. P., Winklhofer, M., Kodama, K. P., & Horg, C. S. (2010). Detection of noninteracting single domain particles using first-order reversal curve diagrams. *Geochemistry, Geophysics, Geosystems*, *11*(1), Q01Z11. <https://doi.org/10.1029/2009GC002916>
- Egli, R., & Lowrie, W. (2002). Anhyseretic remanent magnetization of fine magnetic particles. *Journal of Geophysical Research*, *107*(B10), 2209. <https://doi.org/10.1029/2001JB000671>
- Evans, M. E., & Heller, F. (2003). *Environmental magnetism: Principles and applications of enviromagnetics*. Academic Press.
- Fabian, K., & Leonhardt, R. (2009). Records of paleomagnetic field variations. In *Geomagnetic Field Variations* (pp. 65–106). Springer. [https://doi.org/10.1007/978-3-540-76939-2\\_3](https://doi.org/10.1007/978-3-540-76939-2_3)
- Faivre, D., & Schüler, D. (2008). Magnetotactic bacteria and magnetosomes. *Chemical Reviews*, *108*(11), 4875–4898. <https://doi.org/10.1021/cr078258w>
- Florindo, F., Farmer, R. K., Harwood, D. M., Cody, R. D., Levy, R., Bohaty, S. M., et al. (2013). Paleomagnetism and biostratigraphy of sediments from Southern Ocean ODP Site 744 (southern Kerguelen Plateau): Implications for early-to-middle Miocene climate in Antarctica. *Global and Planetary Change*, *110*, 434–454. <https://doi.org/10.1016/j.gloplacha.2013.05.004>
- Fortin, D., & Langley, S. (2005). Formation and occurrence of biogenic iron-rich minerals. *Earth-Science Reviews*, *72*, 1–19. <https://doi.org/10.1016/j.earscirev.2005.03.002>
- Franke, C., Dobeneck, T., Drury, M. R., Meeldijk, J. D., & Dekkers, M. J. (2007). Magnetic petrology of equatorial Atlantic sediments: Electron microscopy results and their implications for environmental magnetic interpretation. *Paleoceanography*, *22*(4). <https://doi.org/10.1029/2007pa001442>
- Ge, S., Shi, X., Liu, Y., Wang, K., Zou, J., Diao, J., et al. (2012). Turbidite and bottom-current evolution revealed by anisotropy of magnetic susceptibility of redox sediments in the Ulleung Basin, Sea of Japan. *Chinese Science Bulletin*, *57*(6), 660–672. <https://doi.org/10.1007/s11434-011-4812-5>
- Harrison, R. J., & Feinberg, J. M. (2008). FORCinel: An improved algorithm for calculating first-order reversal curve distributions using locally weighted regression smoothing. *Geochemistry, Geophysics, Geosystems*, *9*(5), Q05016. <https://doi.org/10.1029/2008GC001987>

- Harrison, R. J., Muraszko, J., Heslop, D., Lascu, I., Muxworthy, A. R., & Roberts, A. P. (2018). An improved algorithm for unmixing first-order reversal curve diagrams using principal component analysis. *Geochemistry, Geophysics, Geosystems*, *19*(5), 1595–1610. <https://doi.org/10.1029/2018GC007511>
- Heslop, D. (2015). Numerical strategies for magnetic mineral unmixing. *Earth-Science Reviews*, *150*, 256–284. <https://doi.org/10.1016/j.earscirev.2015.07.007>
- Heslop, D., Roberts, A. P., & Chang, L. (2014). Characterizing magnetofossils from first-order reversal curve (FORC) central ridge signatures. *Geochemistry, Geophysics, Geosystems*, *15*(6), 2170–2179. <https://doi.org/10.1002/2014GC005291>
- Heslop, D., Roberts, A. P., Chang, L., Davies, M., Abrajewitch, A., & De Deckker, P. (2013). Quantifying magnetite magnetofossil contributions to sedimentary magnetizations. *Earth and Planetary Science Letters*, *382*, 58–65. <https://doi.org/10.1016/j.epsl.2013.09.011>
- Hesse, P. P. (1994). Evidence for bacterial palaeoecological origin of mineral magnetic cycles in oxic and sub-oxic Tasman Sea sediments. *Marine Geology*, *117*, 1–17. [https://doi.org/10.1016/0025-3227\(94\)90003-5](https://doi.org/10.1016/0025-3227(94)90003-5)
- Hunt, C. P., Banerjee, S. K., Han, J., Solheid, P. A., Oches, E., Sun, W., & Liu, T. (1995). Rock-magnetic proxies of climate change in the loess-palaeosol sequences of the western Loess Plateau of China. *Geophysical Journal International*, *123*(1), 232–244. <https://doi.org/10.1111/j.1365-246X.1995.tb06672.x>
- Inoue, K., Yamazaki, T., & Usui, Y. (2021). Influence of magnetofossils on paleointensity estimations inferred from principal component analyses of first-order reversal curve diagrams for sediments from the Western Equatorial Pacific. *Geochemistry, Geophysics, Geosystems*, *22*(10), e2021GC010081. <https://doi.org/10.1029/2021GC010081>
- Johnson, H. P., Lowrie, W., & Kent, D. V. (1975). Stability of anhysteretic remanent magnetization in fine and coarse magnetite and maghemite particles. *Geophysical Journal of the Royal Astronomical Society*, *41*(1), 1–10. <https://doi.org/10.1111/j.1365-246X.1975.tb05480.x>
- Just, J., Dekkers, M. J., Dobeneck, T., Hoesel, A., & Bickert, T. (2012). Signatures and significance of aeolian, fluvial, bacterial and diagenetic magnetic mineral fractions in Late Quaternary marine sediments off Gambia, NW Africa. *Geochemistry, Geophysics, Geosystems*, *13*(9). <https://doi.org/10.1029/2012gc004146>
- King, J., Banerjee, S. K., Marvin, J., & Özdemir, Ö. (1982). A comparison of different magnetic methods for determining the relative grain size of magnetite in natural materials: Some results from lake sediments. *Earth and Planetary Science Letters*, *59*(2), 404–419. <https://doi.org/10.1029/JB088iB07p05911>
- King, J. W., Banerjee, S. K., & Marvin, J. (1983). A new rock-magnetic approach to selecting sediments for geomagnetic paleointensity studies: Application to paleointensity for the last 4000 years. *Journal of Geophysical Research*, *88*(B7), 5911–5921. <https://doi.org/10.1029/JB088iB07p05911>
- Kirschvink, J. L., & Chang, S. B. R. (1984). Ultrafine-grained magnetite in deep-sea sediments: Possible bacterial magnetofossils. *Geology*, *12*(9), 559–562. [https://doi.org/10.1130/0091-7613\(1984\)12<559:umidsp>2.0.co;2](https://doi.org/10.1130/0091-7613(1984)12<559:umidsp>2.0.co;2)
- Kopp, R. E., & Kirschvink, J. L. (2008). The identification and biogeochemical interpretation of fossil magnetotactic bacteria. *Earth-Science Reviews*, *86*, 42–61. <https://doi.org/10.1016/j.earscirev.2007.08.001>
- Larrasoña, J. C., Roberts, A. P., Chang, L., Schellenberg, S. A., FitzGerald, J. D., Norris, R. D., & Zachos, J. C. (2012). Magnetotactic bacterial response to Antarctic dust supply during the Palaeocene–Eocene thermal maximum. *Earth and Planetary Science Letters*, *333*, 122–133. <https://doi.org/10.1016/j.epsl.2012.04.003>
- Lascu, I., Einsle, J. F., Ball, M. R., & Harrison, R. J. (2018). The vortex state in geologic materials: A micromagnetic perspective. *Journal of Geophysical Research: Solid Earth*, *123*(9), 7285–7304. <https://doi.org/10.1029/2018JB015909>
- Lascu, I., Harrison, R. J., Li, Y., Muraszko, J. R., Channell, J. E. T., Piotrowski, A. M., & Hodell, D. A. (2015). Magnetic unmixing of first-order reversal curve diagrams using principal component analysis. *Geochemistry, Geophysics, Geosystems*, *16*(9), 2900–2915. <https://doi.org/10.1002/2015GC005909>
- Lean, C. M. B., & McCave, I. N. (1998). Glacial to interglacial mineral magnetic and palaeoceanographic changes at Chatham Rise, SW Pacific Ocean. *Earth and Planetary Science Letters*, *163*, 247–260. [https://doi.org/10.1016/S0012-821X\(98\)00191-5](https://doi.org/10.1016/S0012-821X(98)00191-5)
- Levi, S., & Merrill, R. T. (1976). A comparison of ARM and TRM in magnetite. *Earth and Planetary Science Letters*, *32*(2), 171–184. [https://doi.org/10.1016/0012-821X\(76\)90056-X](https://doi.org/10.1016/0012-821X(76)90056-X)
- Li, J., Liu, Y., Liu, S., Roberts, A. P., Pan, H., Xiao, T., & Pan, Y. (2020). Classification of a complexly mixed magnetic mineral assemblage in Pacific Ocean surface sediment by electron microscopy and supervised magnetic unmixing. *Frontiers of Earth Science*, *8*, 609058. <https://doi.org/10.3389/feart.2020.609058>
- Li, J., Wu, W., Liu, Q., & Pan, Y. (2012). Magnetic anisotropy, magnetostatic interactions and identification of magnetofossils. *Geochemistry, Geophysics, Geosystems*, *13*(12). <https://doi.org/10.1029/2012gc004384>
- Li, Q., Zhang, Q., Li, G., Liu, Q., Chen, M. T., Xu, J., & Li, J. (2019). A new perspective for the sediment provenance evolution of the middle Okinawa Trough since the last deglaciation based on integrated methods. *Earth and Planetary Science Letters*, *528*, 115839. <https://doi.org/10.1016/j.epsl.2019.115839>
- Li, X. H., Wei, G., Shao, L., Liu, Y., Liang, X., Jian, Z., et al. (2003). Geochemical and Nd isotopic variations in sediments of the South China Sea: A response to Cenozoic tectonism in SE Asia. *Earth and Planetary Science Letters*, *211*, 207–220. [https://doi.org/10.1016/S0012-821X\(03\)00229-2](https://doi.org/10.1016/S0012-821X(03)00229-2)
- Liu, J., Shi, X., Liu, Y., Liu, Q., Liu, Y., Zhang, Q., et al. (2019). A thick negative polarity anomaly in a sediment core from the central Arctic Ocean: Geomagnetic excursion versus reversal. *Journal of Geophysical Research: Solid Earth*, *124*(11), 10687–10703. <https://doi.org/10.1029/2019JB018073>
- Lovley, D. R., Stolz, J. F., Nord, G. L., & Phillips, E. J. (1987). Anaerobic production of magnetite by a dissimilatory iron-reducing microorganism. *Nature*, *330*(6145), 252–254. <https://doi.org/10.1038/330252a0>
- Ludwig, P., Egli, R., Bishop, S., Chernenko, V., Frederichs, T., Rugele, G., et al. (2013). Characterization of primary and secondary magnetite in marine sediment by combining chemical and magnetic unmixing techniques. *Global and Planetary Change*, *110*, 321–339. <https://doi.org/10.1016/j.gloplacha.2013.08.018>
- Lyle, M., Wilson, P. A., & Janecek, T. R. (2002). Site 1218. *Proceedings of the Ocean Drilling Program, Initial Reports*, *199*, 1–126. <https://doi.org/10.2973/odp.proc.ir.199.111.2002>
- Macrì, P., Sagnotti, L., Dinarès-Turell, J., & Caburlotto, A. (2005). A composite record of Late Pleistocene relative geomagnetic paleointensity from the Wilkes Land Basin (Antarctica). *Physics of the Earth and Planetary Interiors*, *151*, 223–242. <https://doi.org/10.1016/j.pepi.2005.03.004>
- Maher, B. A. (1988). Magnetic properties of some synthetic sub-micron magnetites. *Geophysical Journal International*, *94*(1), 83–96. <https://doi.org/10.1111/j.1365-246X.1988.tb03429.x>
- Maher, B. A. (2011). The magnetic properties of Quaternary aeolian dusts and sediments, and their palaeoclimatic significance. *Aeolian Research*, *3*(2), 87–144. <https://doi.org/10.1016/j.aeolia.2011.01.005>

- Miot, J., Benzerara, K., Morin, G., Kappler, A., Bernard, S., Obst, M., et al. (2009). Iron biomineralization by anaerobic neutrophilic iron-oxidizing bacteria. *Geochimica et Cosmochimica Acta*, 73(3), 696–711. <https://doi.org/10.1016/j.gca.2008.10.033>
- Moskowitz, B. M., Frankel, R. B., & Bazylinski, D. A. (1993). Rock magnetic criteria for the detection of biogenic magnetite. *Earth and Planetary Science Letters*, 120, 283–300. [https://doi.org/10.1016/0012-821X\(93\)90245-5](https://doi.org/10.1016/0012-821X(93)90245-5)
- Nie, J., Song, Y., King, J. W., Zhang, R., & Fang, X. (2013). Six million years of magnetic grain-size records reveal that temperature and precipitation were decoupled on the Chinese Loess Plateau during ~4.5–2.6 Ma. *Quaternary Research*, 79(3), 465–470. <https://doi.org/10.1016/j.yqres.2013.01.002>
- Oldfield, F. (2007). Sources of fine-grained magnetic minerals in sediments: A problem revisited. *The Holocene*, 17(8), 1265–1271. <https://doi.org/10.1177/095959683607085135>
- Pan, Y., Petersen, N., Winkhofer, M., Davila, A. F., Liu, Q., Frederichs, T., et al. (2005). Rock magnetic properties of uncultured magnetotactic bacteria. *Earth and Planetary Science Letters*, 237, 311–325. <https://doi.org/10.1016/j.epsl.2005.06.029>
- Pan, Y., Zhu, R., Shaw, J., Liu, Q., & Guo, B. (2001). Can relative paleointensities be determined from the normalized magnetization of the wind-blown loess of China? *Journal of Geophysical Research*, 106(B9), 19221–19232. <https://doi.org/10.1029/2001JB000360>
- Pike, C. R., Roberts, A. P., & Verosub, K. L. (1999). Characterizing interactions in fine magnetic particle systems using first order reversal curves. *Journal of Applied Physics*, 85(9), 6660–6667. <https://doi.org/10.1063/1.370176>
- Pike, C. R., Roberts, A. P., & Verosub, K. L. (2001). First order reversal curve diagrams and thermal relaxation effects in magnetic particles. *Geophysical Journal International*, 145(3), 721–730. <https://doi.org/10.1046/j.0956-540x.2001.01419.x>
- Qian, Y., Roberts, A. P., Liu, Y., Hu, P., Zhao, X., Heslop, D., et al. (2020). Assessment and integration of bulk and component-specific methods for identifying mineral magnetic assemblages in environmental magnetism. *Journal of Geophysical Research: Solid Earth*, 125(8), e2019JB019024. <https://doi.org/10.1029/2019JB019024>
- Richter, C., Venuti, A., Verosub, K. L., & Wei, K. Y. (2006). Variations of the geomagnetic field during the Holocene: Relative paleointensity and inclination record from the West Pacific (ODP Hole 1202B). *Physics of the Earth and Planetary Interiors*, 156, 179–193. <https://doi.org/10.1016/j.pepi.2005.08.006>
- Roberts, A. P., Almeida, T. P., Church, N. S., Harrison, R. J., Heslop, D., Li, Y., et al. (2017). Resolving the origin of pseudo-single domain magnetic behavior. *Journal of Geophysical Research: Solid Earth*, 122(12), 9534–9558. <https://doi.org/10.1002/2017JB014860>
- Roberts, A. P., Chang, L., Heslop, D., Florindo, F., & Larrasoana, J. C. (2012). Searching for single domain magnetite in the “pseudo-single-domain” sedimentary haystack: Implications of biogenic magnetite preservation for sediment magnetism and relative paleointensity determinations. *Journal of Geophysical Research*, 117(B8). <https://doi.org/10.1029/2012JB009412>
- Roberts, A. P., Florindo, F., Villa, G., Chang, L., Jovane, L., Bohaty, S. M., et al. (2011). Magnetotactic bacterial abundance in pelagic marine environments is limited by organic carbon flux and availability of dissolved iron. *Earth and Planetary Science Letters*, 310, 441–452. <https://doi.org/10.1016/j.epsl.2011.08.011>
- Roberts, A. P., Pike, C. R., & Verosub, K. L. (2000). First-order reversal curve diagrams: A new tool for characterizing the magnetic properties of natural samples. *Journal of Geophysical Research*, 105(B12), 28461–28475. <https://doi.org/10.1029/2000JB900326>
- Roberts, A. P., Tauxe, L., & Heslop, D. (2013). Magnetic paleointensity stratigraphy and high-resolution Quaternary geochronology: Successes and future challenges. *Quaternary Science Reviews*, 61, 1–16. <https://doi.org/10.1016/j.quascirev.2012.10.036>
- Roberts, A. P., Zhao, X., Harrison, R. J., Heslop, D., Muxworthy, A. R., Rowan, C. J., et al. (2018). Signatures of reductive magnetic mineral diagenesis from unmixing of first-order reversal curves. *Journal of Geophysical Research: Solid Earth*, 123(6), 4500–4522. <https://doi.org/10.1029/2018JB015706>
- Roberts, A. P., Zhao, X., Hu, P., Abrajevitch, A., Chen, Y. H., Harrison, R. J., et al. (2021). Magnetic Domain State and Anisotropy in Hematite ( $\alpha\text{-Fe}_2\text{O}_3$ ) From First-Order Reversal Curve Diagrams. *Journal of Geophysical Research: Solid Earth*, 126(12), e2021JB023027. <https://doi.org/10.1029/2021JB023027>
- Sakuramoto, Y., Yamazaki, T., Kimoto, K., Miyairi, Y., Kuroda, J., Yokoyama, Y., & Matsuzaki, H. (2017). A geomagnetic paleointensity record of 0.6 to 3.2 Ma from sediments in the western equatorial Pacific and remanent magnetization lock-in depth. *Journal of Geophysical Research: Solid Earth*, 122(10), 7525–7543. <https://doi.org/10.1002/2017JB014450>
- Sparks, N. H. C., Mann, S., Bazylinski, D. A., Lovley, D. R., Jannasch, H. W., & Frankel, R. B. (1990). Structure and morphology of magnetite anaerobically-produced by a marine magnetotactic bacterium and a dissimilatory iron-reducing bacterium. *Earth and Planetary Science Letters*, 98(1), 14–22. [https://doi.org/10.1016/0012-821X\(90\)90084-b](https://doi.org/10.1016/0012-821X(90)90084-b)
- Stolz, J. F., Chang, S. B. R., & Kirschvink, J. L. (1986). Magnetotactic bacteria and single-domain magnetite in hemipelagic sediments. *Nature*, 321(6073), 849–851. <https://doi.org/10.1038/321849a0>
- Stoner, J. S., Channell, J. E. T., Hillaire-Marcel, C., & Kissel, C. (2000). Geomagnetic paleointensity and environmental record from Labrador Sea core MD95-2024: Global marine sediment and ice core chronostratigraphy for the last 110 kyr. *Earth and Planetary Science Letters*, 183, 161–177. [https://doi.org/10.1016/S0012-821X\(00\)00272-7](https://doi.org/10.1016/S0012-821X(00)00272-7)
- Stoner, J. S., Channell, J. E. T., Hodell, D. A., & Charles, C. D. (2003). A ~580 kyr paleomagnetic record from the sub-Antarctic South Atlantic (Ocean Drilling Program Site 1089). *Journal of Geophysical Research*, 108(B5). <https://doi.org/10.1029/2001JB001390>
- Tarduno, J. A., Tian, W., & Wilkison, S. (1998). Biogeochemical remanent magnetization in pelagic sediments of the western equatorial Pacific Ocean. *Geophysical Research Letters*, 25(21), 3987–3990. <https://doi.org/10.1029/1998GL900079>
- Tauxe, L. (1993). Sedimentary records of relative paleointensity of the geomagnetic field: Theory and practice. *Reviews of Geophysics*, 31(3), 319–354. <https://doi.org/10.1029/93RG01771>
- Tauxe, L., Pick, T., & Kok, Y. S. (1995). Relative paleointensity in sediments: A pseudo-Thellier approach. *Geophysical Research Letters*, 22(21), 2885–2888. <https://doi.org/10.1029/95GL03166>
- Tauxe, L., & Yamazaki, T. (2015). Paleointensities. In G. Schubert (Ed.), *Treatise on Geophysics* (pp. 461–509). Elsevier. <https://doi.org/10.1016/b978-0-444-53802-4.00107-x>
- Thompson, R., & Oldfield, F. (1986). Environmental Magnetism. In *Environmental magnetism*. Allen and Unwin. <https://doi.org/10.1007/978-94-011-8036-8>
- Torrent, J., Liu, Q., Bloemendal, J., & Barrón, V. (2007). Magnetic enhancement and iron oxides in the upper Luochuan loess–paleosol sequence, Chinese Loess Plateau. *Soil Science Society of America Journal*, 71(5), 1570–1578. <https://doi.org/10.2136/sssaj2006.0328>
- Vali, H., Förster, O., Amarantidis, G., & Petersen, N. (1987). Magnetotactic bacteria and their magnetofossils in sediments. *Earth and Planetary Science Letters*, 86, 389–400. [https://doi.org/10.1016/0012-821X\(87\)90235-4](https://doi.org/10.1016/0012-821X(87)90235-4)
- Vali, H., Von Dobeneck, T., Amarantidis, G., Förster, O., Morteani, G., Bachmann, L., & Petersen, N. (1989). Biogenic and lithogenic magnetic minerals in Atlantic and Pacific deep sea sediments and their paleomagnetic significance. *Geologische Rundschau*, 78(3), 753–764. <https://doi.org/10.1007/bf01829320>
- Von Dobeneck, T., Petersen, N., & Vali, H. (1987). Bakterielle magnetofossilien. *Geowissenschaften in Unserer Zeit*, 1, 27–35.

- Wagner, C. L., Lascu, I., Lippert, P. C., Egli, R., Livi, K. J., & Sears, H. B. (2021). Diversification of iron-biomineralizing organisms during the Paleocene-Eocene Thermal Maximum: Evidence from quantitative unmixing of magnetic signatures of conventional and giant magnetofossils. *Paleoceanography and Paleoclimatology*, *36*(5), e2021PA004225. <https://doi.org/10.1029/2021PA004225>
- Wan, S., Li, A., Clift, P. D., & Stuet, J. B. W. (2007). Development of the East Asian monsoon: Mineralogical and sedimentologic records in the northern South China Sea since 20 Ma. *Paleoceanography, Palaeoclimatology, Palaeoecology*, *254*, 561–582. <https://doi.org/10.1016/j.palaeo.2007.07.009>
- Wang, H., Xu, X., Liu, Q., Zhong, Y., Chen, T., Qiang, X., et al. (2020). Geomagnetic paleointensity and its geodynamic significance for the last 40 ka recorded in the northwestern sub-sea basin of the South China Sea. *Chinese Journal of Geophysics*, *63*(7), 2671–2681. <https://doi.org/10.6038/cjg2020N0353>
- Wu, L., Wang, R., Xiao, W., Ge, S., Chen, Z., & Krijgsman, W. (2017). Productivity-climate coupling recorded in Pleistocene sediments off Prydz Bay (East Antarctica). *Paleoceanography, Palaeoclimatology, Palaeoecology*, *485*, 260–270. <https://doi.org/10.1016/j.palaeo.2017.06.018>
- Yamamoto, Y., Yamazaki, T., Kanamatsu, T., Ioka, N., & Mishima, T. (2007). Relative paleointensity stack during the last 250 kyr in the north-west Pacific. *Journal of Geophysical Research*, *112*(B1), B01104. <https://doi.org/10.1029/2006JB004477>
- Yamazaki, T. (2012). Paleoposition of the Intertropical Convergence Zone in the eastern Pacific inferred from glacial-interglacial changes in terrigenous and biogenic magnetic mineral fractions. *Geology*, *40*(2), 151–154. <https://doi.org/10.1130/G32646.1>
- Yamazaki, T., Fu, W., Shimono, T., & Usui, Y. (2020). Unmixing biogenic and terrigenous magnetic mineral components in red clay of the Pacific Ocean using principal component analyses of first-order reversal curve diagrams and paleoenvironmental implications. *Earth Planets and Space*, *72*(1), 1–15. <https://doi.org/10.1186/s40623-020-01248-5>
- Yamazaki, T., & Horiuchi, K. (2016). Precessional control on ocean productivity in the Western Pacific Warm Pool for the last 400 kyr: Insight from biogenic magnetite. *Geochemistry, Geophysics, Geosystems*, *17*(11), 4399–4412. <https://doi.org/10.1002/2016GC006446>
- Yamazaki, T., & Ikehara, M. (2012). Origin of magnetic mineral concentration variation in the Southern Ocean. *Paleoceanography*, *27*(2), PA2206. <https://doi.org/10.1029/2011PA002271>
- Yamazaki, T., & Shimono, T. (2013). Abundant bacterial magnetite occurrence in oxic red clay. *Geology*, *41*(11), 1191–1194. <https://doi.org/10.1130/G34782.1>
- Yamazaki, T., Suzuki, Y., Kouduka, M., & Kawamura, N. (2019). Dependence of bacterial magnetosome morphology on chemical conditions in deep-sea sediments. *Earth and Planetary Science Letters*, *513*, 135–143. <https://doi.org/10.1016/j.epsl.2019.02.015>
- Yamazaki, T., & Yamamoto, Y. (2018). Relative paleointensity and inclination anomaly over the last 8 Myr obtained from the Integrated Ocean Drilling Program Site U1335 sediments in the Eastern Equatorial Pacific. *Journal of Geophysical Research: Solid Earth*, *123*(9), 7305–7320. <https://doi.org/10.1029/2018JB016209>
- Zhang, Q., Liu, Q., Li, J., & Sun, Y. (2018). An integrated study of the eolian dust in pelagic sediments from the North Pacific Ocean based on environmental magnetism, transmission electron microscopy, and diffuse reflectance spectroscopy. *Journal of Geophysical Research: Solid Earth*, *123*(5), 3358–3376. <https://doi.org/10.1002/2017JB014951>
- Zhang, Q., Liu, Q., Roberts, A. P., Yu, J., Liu, Y., & Li, J. (2021). Magnetotactic bacterial activity in the North Pacific Ocean and its relationship to Asian dust inputs and primary productivity since 8.0 Ma. *Geophysical Research Letters*, *48*(15), e2021GL094687. <https://doi.org/10.1029/2021GL094687>
- Zhu, R., Guo, B., Pan, Y., Liu, Q., Zeman, A., & Suchy, V. (2000). Reliability of geomagnetic secular variations recorded in a loess section at Lingtai, north-central China. *Science in China, Series A D*, *43*(1), 1–9. <https://doi.org/10.1007/BF02877826>